The Optical Stretcher: A Novel Laser Tool to Micromanipulate Cells

Jochen Guck,* Revathi Ananthakrishnan,* Hamid Mahmood,* Tess J. Moon,[†¶] C. Casey Cunningham,[‡] and Josef Käs*[§¶‖]

*Center for Nonlinear Dynamics, Department of Physics, University of Texas at Austin, Texas 78712, [†]Department of Mechanical Engineering, University of Texas at Austin, Texas 78712, [‡]Baylor University Medical Center, Dallas, Texas 75246, [§]Institute for Molecular and Cellular Biology, University of Texas at Austin, Texas 78712, [¶]Texas Materials Institute, University of Texas at Austin, Texas 78712, [‖]Center for Nano- and Molecular Science and Technology, University of Texas, Austin, Texas 78712 USA

ABSTRACT   When a dielectric object is placed between two opposed, nonfocused laser beams, the total force acting on the object is zero but the surface forces are additive, thus leading to a stretching of the object along the axis of the beams. Using this principle, we have constructed a device, called an optical stretcher, that can be used to measure the viscoelastic properties of dielectric materials, including biologic materials such as cells, with the sensitivity necessary to distinguish even between different individual cytoskeletal phenotypes. We have successfully used the optical stretcher to deform human erythrocytes and mouse fibroblasts. In the optical stretcher, no focusing is required, thus radiation damage is minimized and the surface forces are not limited by the light power. The magnitude of the deforming forces in the optical stretcher thus bridges the gap between optical tweezers and atomic force microscopy for the study of biologic materials.

INTRODUCTION

For almost three decades, laser traps have been used to manipulate objects ranging in size from atoms to cells (Ashkin, 1970; Chu, 1991; Svoboda and Block, 1994). The basic principle of laser traps is that momentum is transferred from the light to the object, which in turn, by Newton's second law, exerts a force on the object. Thus far, these optical forces have solely been used to trap an object. The most common laser trap is a one-beam gradient trap, called optical tweezers (Ashkin et al., 1986). Optical tweezers have been an invaluable tool in cell biological research: for trapping cells (Ashkin et al., 1987; Ashkin and Dziedzic, 1987), measuring forces exerted by molecular motors such as myosin or kinesin (Block et al., 1990; Shepherd et al., 1990; Kuo and Sheetz, 1993; Simmons et al., 1993; Svoboda et al., 1993), or the swimming forces of sperm (Tadir et al., 1990; Colon et al., 1992), and for studying the polymeric properties of single DNA strands (Chu, 1991).

In contrast, the optical stretcher is based on a double-beam trap (Ashkin, 1970; Constable et al., 1993) in which two opposed, slightly divergent, and identical laser beams with Gaussian intensity profile trap an object in the middle. This trapping is stable if the total force on the object is zero and restoring. This condition is fulfilled if the refractive index of the object is larger than the refractive index of the surrounding medium and if the beam sizes are larger than the size of the trapped object. In extended objects such as cells, the momentum transfer primarily occurs at the surface. The total force acting on the center of gravity is zero because the two-beam trap geometry is symmetric and all

the resulting surface forces cancel. Nevertheless, if the object is sufficiently elastic, the surface forces stretch the object along the beam axis (see Fig. 1) (Guck et al., 2000). At first, this optical stretching may seem counterintuitive, but it can be explained in a simple way. It is well known that light carries momentum. Whenever a ray of light is reflected or refracted at an interface between media with different refractive indices, changing direction or velocity, its momentum changes. Because momentum is conserved, some momentum is transferred from the light to the interface and, by Newton's second law, a force is exerted on the interface.

To illustrate, let us consider a ray of light passing through a cube of optically denser material (see Fig. 2). As it enters the dielectric object, the light gains momentum so that the surface gains momentum in the opposite (backward) direction. Similarly, the light loses momentum upon leaving the dielectric object so that the opposite surface gains momentum in the direction of the light propagation. The reflection of light on either surface also leads to momentum transfer on both surfaces in the direction of light propagation. This contribution to the surface forces is smaller than the contribution that stems from the increase of the light's momentum inside the cube. The two resulting surface forces on front and backside are opposite and tend to stretch the object (Guck et al., 2000). However, the asymmetry between the surface forces leads to a total force that acts on the center of the cube. If there is a second, identical ray of light that passes through the cube from the opposite side, there is no total force on the cube, but the forces on the surface generated by the two rays are additive. In contrast to asymmetric trapping geometries, where the total force is the trapping force used in optical traps, the optical stretcher exploits surface forces to stretch objects. Light powers as high as 800 mW in each beam can be used, which lead to surface forces up to hundreds of pico-Newton. There is no problem with radiation damage to the cells examined, which is not surprising because the laser beams in the optical stretcher
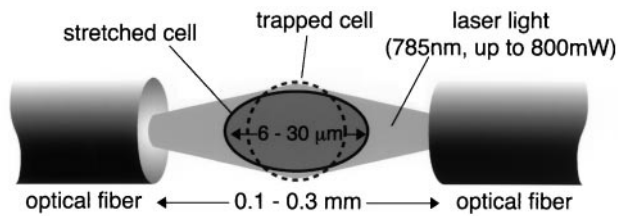
FIGURE 1 Schematic of the stretching of a cell trapped in the optical stretcher. The cell is stably trapped in the middle by the optical forces from the two laser beams. Depending on the elastic strength of the cell, at a certain light power the cell is stretched out along the laser beam axis. The drawing is not to scale; the diameter of the optical fibers is $125 \pm 5 \, \mu$m.

are not focused, minimizing the light flux through the cells in comparison to other optical traps (see Viability of Stretched Cells). To demonstrate this concept of optical deformability, we stretched osmotically swollen erythrocytes and BALB 3T3 fibroblasts.

Human erythrocytes, i.e., red blood cells (RBCs), were used as initial test objects. Red blood cells offer several advantages as a model system for this type of experiment in that they lack any internal organelles, are homogeneously filled with hemoglobin, and can be osmotically swollen to a spherical shape. They are thus close to the model of an isotropic, soft, dielectric sphere without internal structure that we used for the calculation of the stress profiles (see below). Furthermore, they are very soft cells and deformations are easily observed. As an additional advantage, RBCs have been studied extensively and their elastic properties are well known (Bennett, 1985, 1990; Mohandas and Evans, 1994). The only elastic component of RBCs is a thin membrane composed of a phospholipid bilayer sandwiched between a triagonal network of spectrin filaments on the inside and glycocalix brushes on the outside (Mohandas and Evans, 1994). The ratio between cell radius ρ and membrane thickness h, $\rho/h \approx 100$. This means that the bending energy is negligibly small compared to the stretching energy (see Deformation of Thin Shells). Thus, linear membrane theory can be used to predict the deformations of RBCs subjected to the surface stresses in the optical stretcher. By comparing the deformations observed in the optical stretcher with the deformations expected, we quantitatively verified the forces predicted from our calculations.

The BALB 3T3 fibroblasts under investigation are an example of typical eukaryotic cells that, in contrast to RBCs, have an extensive three-dimensional (3D) network of protein filaments throughout the cytoplasm as the main elastic component (Lodish et al., 1995). In this network, called the cytoskeleton, semiflexible actin filaments, rod-like microtubules, and flexible intermediate filaments are arranged into an extensive, 3D compound material with the help of accessory proteins (Adelman et al., 1968; Pollard, 1984; Elson, 1988; Janmey, 1991). Classical concepts in polymer physics fail to explain how these filaments provide
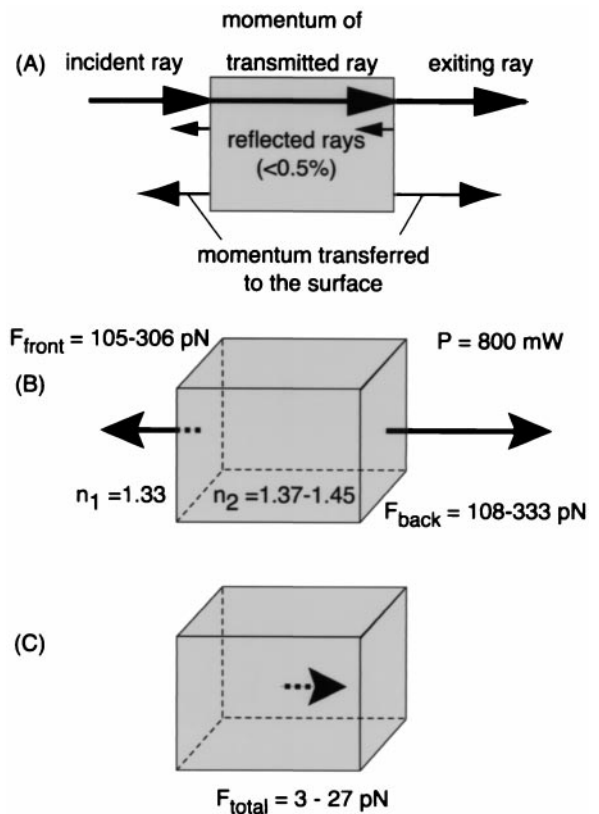

FIGURE 2 Momentum transfer and resulting forces on a dielectric box due to one laser beam incident from the left. (*A*) A small portion of the incident light is reflected at the front surface. The rest enters the box and gains momentum due to the higher refractive index inside. On the back, the same fraction is reflected and the exiting light loses momentum. The lower arrows indicate the momentum transferred to the surface. (*B*) The resulting forces for a light power of 800 mW at the front and the back are $F_{\text{front}} = 105$–306 pN and $F_{\text{back}} = 108$–333 pN, respectively, depending on the refractive index of the material. Note that the force on the back is larger than the force on the front. (*C*) Due to the difference between forces on front and back, there is a total force, $F_{\text{total}} = F_{\text{back}} - F_{\text{front}} = 3 - 27$ pN, acting on the center of gravity of the box. This total force pushes the box away from the light source. An elastic material will be deformed by the forces acting on the surface, which are an order of magnitude larger than the total force.

mechanical stability to cells (MacKintosh et al., 1995), but, in most cells, cytoskeletal actin is certainly a main determinant of mechanical strength and stability (Stossel, 1984, Janmey et al., 1986; Sato et al., 1987; Elson, 1988).

The actin cortex is a thick ($\rho/h \approx 10$) homogeneous layer just beneath the plasma membrane. In cells adhered to the substrate, additional bundles of individual actin filaments, called stress fibers, insert into focal adhesion plaques and span the entire cell interior. Dynamic remodeling of this network of F-actin facilitates such important cell functions as motility and the cytoplasmic cleavage as the last step of mitosis (Pollard, 1986; Carlier, 1998; Stossel et al., 1999). Cells are drastically softened by actin-disrupting cytochalasins (Petersen et al., 1982; Pasternak and Elson, 1985) and

gelsolin (Cooper et al., 1987), indicating the importance of actin. More recently, frequency-dependent atomic force microscopy (AFM)-based microrheology showed that fibroblasts exhibit the same viscoelastic signature as homogeneous actin networks in vitro (Mahaffy et al., 2000). Another experiment (Heidemann et al., 1999) investigated the response of rat embryo fibroblasts to mechanical deformation by glass needles. Actin and microtubules were tagged with green fluorescent protein and the role of these two cytoskeletal components in determining cell shape during deformation was directly visualized. Again, actin was found to be almost exclusively responsible for the cell's elastic response, whereas microtubules clearly showed fluid-like behavior.

In nonmitotic cells, microtubules radiate outward from the microtubule-organizing center just outside the cell nucleus (Lodish et al., 1995). They serve as tracks for the motor proteins dynein and kinesin to transport vesicles through the cell. Microtubules are also required for the separation of chromosomes during mitosis (Mitchison et al., 1986; Mitchison, 1992). Intermediate filaments are unique to multicellular organisms and comprise an entire class of flexible polymers that are specific to certain differentiated cell types (Herrmann and Aebi, 1998; Janmey et al., 1998). For example, vimentin is expressed in mesenchymal cells (e.g., fibroblasts). Vimentin fibers terminate at the nuclear membrane and at desmosomes, or adhesion plaques, on the plasma membrane. Another type of intermediate filament is lamin, which makes up the nuclear lamina, a polymer cortex underlying the nuclear membrane (Aebi et al., 1986). Intermediate filaments are often colocalized with microtubules, suggesting a close association between the two filament networks. Both microtubules and intermediate filaments are thought to be less important for the elastic strength and structural response of cells subjected to external stress (Petersen et al., 1982; Pasternak and Elson, 1985; Heidemann et al., 1999; Rotsch and Radmacher, 2000). However, intermediate filaments become more important at large deformations that cannot be achieved with deforming stresses of several Pascal. Intermediate filaments are also more important to elasticity in adhered cells as opposed to suspended cells, where the initially fully extended filaments become slack (Janmey et al., 1991; Wang and Stamenovic, 2000). Despite these experiments, a quantitative description of the cytoskeletal contribution to a cell's viscoelasticity is still missing. The optical stretcher can be used to measure the viscoelastic properties of the entire cytoskeleton and to shed new light on the problem of cellular elasticity.

The ability to withstand deforming stresses is crucial for cells and has motivated the development of several techniques to investigate cell elasticity. Atomic force microscopy (Radmacher et al., 1996), manipulation with microneedles (Felder and Elson, 1990), microplate manipulation (Thoumine and Ott, 1997), and cell poking (Dailey et al., 1984) are not able to detect small variations in cell elasticity because these detection devices have a very high spring constant compared to the elastic modulus of the material probed. The AFM technique has recently been improved for cell elasticity measurements by attaching micron-sized beads to the scanning tip to reduce the pressure applied to the cell (Mahaffy et al., 2000). Micropipette aspiration of cell segments (Discher et al., 1994) and displacement of surface-attached microspheres (Wang et al., 1993) can provide inaccurate measurements if the plasma membrane becomes detached from the cytoskeleton during deformation. In addition, all of these techniques are very tedious and only probe the elasticity over a relatively small area of a cell's surface. Whole-cell elasticity can be indirectly determined by measurements of the compression and shear moduli of densely packed cell pellets (Elson, 1988; Eichinger et al., 1996), or by using microarray assays (Carlson et al., 1997). However, these measurements only represent an average value rather than a true single-cell measurement, and depend on noncytoskeletal forces such as cell–cell and cell–substrate adhesion. The optical stretcher is a new tool that not only circumvents most of these problems, but also permits the handling of large numbers of individual cells by incorporation of an automated flow chamber, fabricated with modern soft lithography techniques, that guides cells through the detector.

MATERIALS AND METHODS

Erythrocyte preparation

The buffer for the RBCs was derived from Zeman (1989) and Strey et al. (1995) and consisted of 100 mM NaCl, 20 mM Hepes buffer (pH 7.4), 25 mM glucose, 5 mM KCl, 3 mM $CaCl_2$, 2 mM $MgCl_2$, 0.1 mM adenine, 0.1 mM inosine, 1% (volume) antibiotic-antimycotic solution, 0.25–1.5% albumin, and 5 units/ml heparin. All reagents were purchased from Sigma (St. Louis, MO) unless stated otherwise. Red blood cells were obtained by drawing ~10 μl of blood from the earlobe or fingertip. The blood was diluted with 4 ml of the buffer. Because the buffer has a physiological osmolarity (~270 mOsm), the RBCs initially have a flat, biconcave, disc-like shape. However, the buffer was then diluted to lower the osmolarity to 130 mOsm, at which point the RBCs swell to assume a spherical shape. The average radius of the swollen RBCs was measured to be $\rho = 3.13 \pm 0.15$ μm using phase contrast microscopy. The error given is the standard deviation (SD) of 55 cells measured. The refractive index of spherical RBCs, $n = 1.378 \pm 0.005$ (Evans and Fung, 1972), the refractive index of the final buffer was measured to be $n = 1.334 \pm 0.001$, both of which were used for the calculations in the RBC stretching experiments.

Eukaryotic cell preparation

As prototypical eukaryotic cells, BALB 3T3 fibroblasts (CCL-163) were obtained from American Type Culture Collection (Manassas, VA) and maintained in Dulbecco's Modified Eagle's Medium with 10% nonfetal calf serum and 10 mM Hepes at pH 7.4. For cells to be trapped and stretched in the optical stretcher, they must be in suspension. Because these are normally adherent cells, single-cell suspensions for each experiment were obtained by incubating the cells with 0.25% trypsin-EDTA solution at 37°C for 4 min. After detaching, the activity of trypsin-EDTA was inhibited by adding fresh culture medium. This treatment causes the cells
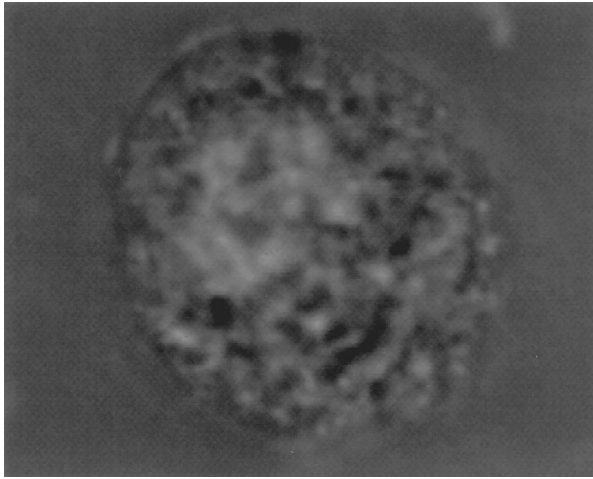
FIGURE 3 Phase contrast image of a BALB 3T3 fibroblast in an albumin solution with refractive index $n = 1.370 \pm 0.005$. At the matching point, the contrast between cell and surrounding is minimal. The lighter parts of the cytoplasm have a slightly lower refractive index, whereas the darker parts have a slightly higher refractive index than the bulk of the cell. The cell's radius is $\rho \approx 8.4 \ \mu$m.

to stay suspended as isolated cells for 2–4 h. Once in suspension, the cells assumed a spherical shape. Their average radius was $\rho = 9.2 \pm 2.8 \ \mu$m (SD of 20 cells measured), and their average refractive index, $n = 1.370 \pm 0.005$, was measured using index matching in phase contrast microscopy (see Fig. 3) (Barer and Joseph, 1954, 1955a,b). The refractive index of the cell medium, which was used for the calculations of the fibroblast shooting and stretching experiments, was measured to be $n = 1.335 \pm 0.002$.

For the fluorescence studies of the actin cytoskeleton of BALB 3T3 cells in suspension, we used TRITC-phalloidin (Molecular Probes, Inc., Eugene, OR), a phallotoxin that binds selectively to filamentous actin (F-actin), increasing the fluorescence quantum yield of the fluorophore rhodamine several-fold over the unbound state (Allen and Janmey, 1994). This assures that predominantly actin filaments are detected rather than actin monomers. Before staining, the cells were spun down and gently resuspended in a 4% formaldehyde solution for 10 min to fix the actin cytoskeleton. They were then washed three times with PBS, permeabilized with a 0.1% Triton-X 100 solution for 2 min, and washed three more times. Then the cells were stained with a 1-μg/ml TRITC-phalloidin solution for 10 min, followed by a final washing step (3× with PBS). Fluorescence images were acquired with an inverted microscope (Axiovert TV100, Carl Zeiss, Inc., Thornwood, NY) and deconvolved using a Jansson–van Cittert algorithm with 100 iterations (Zeiss KS400 software).

Silica and polystyrene beads

The silica and polystyrene beads used for the calibration of the image analysis algorithm and for the shooting experiments were purchased from Bangs Laboratories, Inc. (Fishers, IN). Their radii were $\rho = 2.50 \pm 0.04$ μm (SD) and $\rho = 2.55 \pm 0.04 \ \mu$m (SD), respectively, as given in the specifications provided by the manufacturer. Using index matching, their indices of refraction were measured to be $n = 1.430 \pm 0.003$ for silica beads using mixtures of water and glycerol, and $n = 1.610 \pm 0.005$ for polystyrene beads using mixtures of diethyleneglycolbutylether and α-chloronaphthalene. The index of refraction of water, used for the calculation of the forces on the silica and polystyrene beads in the shooting experiments, was measured to be $n = 1.333 \pm 0.001$.

Experimental setup

The setup of the experiment (see Fig. 4) is essentially a two-beam fiber
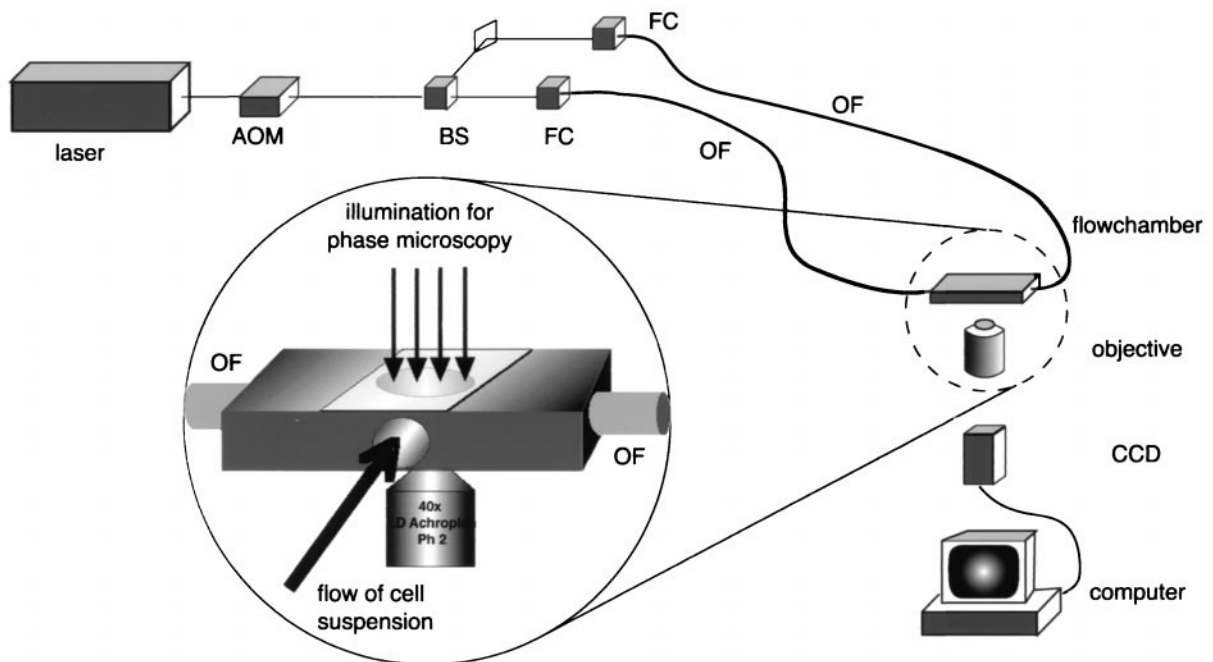

FIGURE 4 Setup of the optical stretcher. The intensity of the laser beam is controlled by the acousto-optic modulator (*AOM*), split in two by a beam splitter (*BS*), and coupled into optical fibers (*OF*) with two fiber couplers (*FC*). The inset shows the flow chamber used to align the fiber tips and to stream a cell suspension through the trapping area. Digital images of the trapping and optical stretching were recorded by a Macintosh computer using a CCD camera.
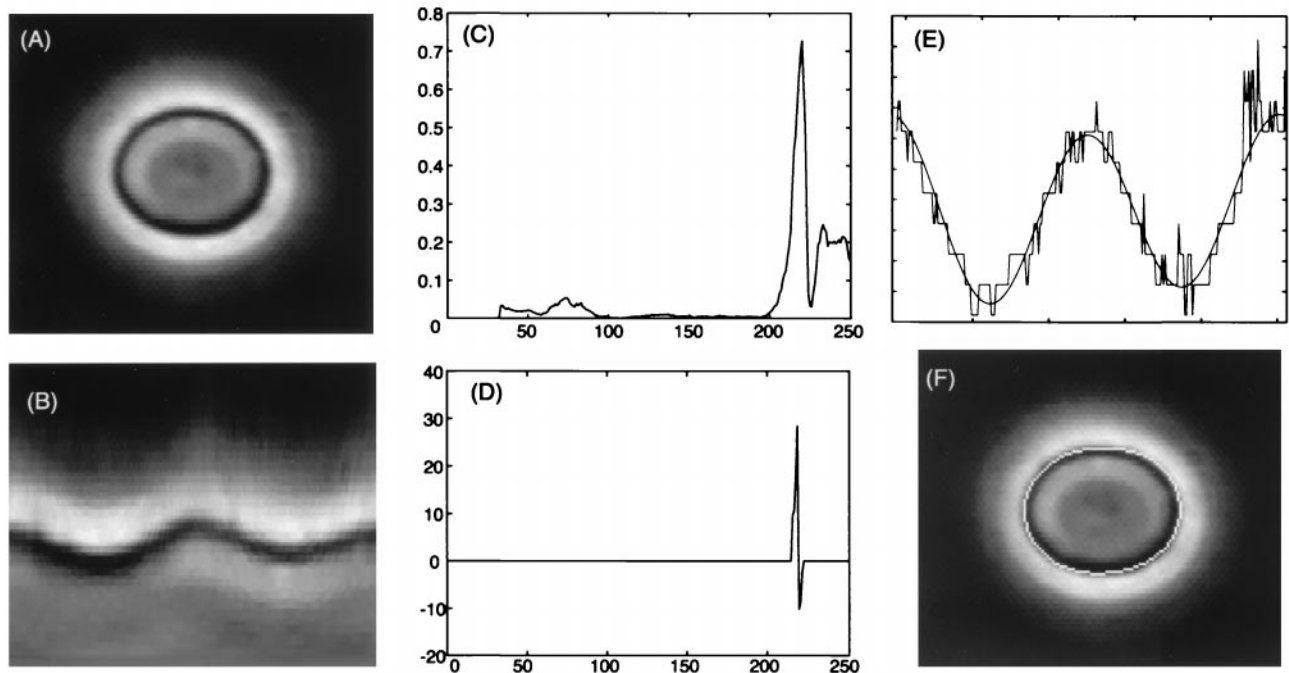
FIGURE 5   Illustration of the algorithm used for the image analysis of the cell deformation in the optical stretcher. (*A*) Original phase contrast image of a stretched spherical RBC. The diameter of the cell is about 6 μm. (*B*) The original image mapped onto a rectangle. The inside of the cell is the lower part of the picture. (*C*) Line scan across the cell boundary from top to bottom after squaring the grayscale values. (*D*) Line scan after thresholding and division by the first spatial derivative. (*E*) The zigzag line is the boundary of the cell as extracted from the binary image. The smooth line is the inverse Fourier transform of the three dominant frequencies in the original data. (*F*) The white line shows the image of this smooth line representing the boundary of the cell as detected by the algorithm converted back into the cell image. The line matches the cell's boundary to a high degree.

trap (Constable et al., 1993). A tunable, cw Ti-Sapphire laser (3900S, Spectra Physics Lasers, Inc., Mountain View, CA) with up to 7W of light power served as light source at a wavelength of $\lambda = 785$ nm (30 GHz bandwidth). An acousto-optic modulator (AOM-802N, IntraAction Corp., Bellwood, IL) was used to control the beam intensity, i.e., the surface forces. This can be done with frequencies between 10^{-2} and 10^{3} Hz, thus allowing for time-dependent rheological measurements in the frequency range most relevant for biological samples. The beam was split in two by a nonpolarizing beam-splitting cube (Newport Corp., Irvine, CA) and then coupled into single-mode optical fibers (mode field diameter $= 5.4 \pm 0.2$ μm, NA 0.11). The fiber couplers were purchased from Oz Optics, Ltd. (Carp, ON, Canada) and the single-mode optical fibers from Newport. The optical fibers not only simplify the setup of the experiment, they also serve as additional spatial filters and guarantee a good spatial mode quality (TEM$_{00}$). The maximum light powers achieved in this setup were 800 mW in each beam at the object trapped. The power exiting the fiber was measured before and after each experimental run to verify the stability of the coupling over the 1–2-h period. All power values given are measured with a relative error of $\pm 1\%$ (SD).

For trapping and stretching cells in the optical stretcher, the fibers' alignment is crucial. For the RBCs, a solution similar to the one described in Constable et al. (1993) was used: a glass capillary with a diameter between 250 and 400 μm was glued onto a microscope slide, and the fibers were pressed alongside so that they were colinear and facing each other (not shown in Fig. 4). Red blood cells were so light that they sunk very slowly and could be trapped out of a cell suspension placed on top of the fiber ends. For the BALB 3T3 fibroblasts, we used a flow chamber geometry (see inset of Fig. 4) that allowed us to stream a suspension of cells directly through the gap between the optical fibers.

After successfully trapping one cell, the flow was stopped and the cell's elasticity was measured. Then the cell was released and the flow was started again until the next cell was trapped. The microscope slide, or the flow chamber, was mounted on an inverted microscope equipped for phase contrast and fluorescence microscopy. Phase contrast images of the trapping and stretching were obtained with a CCD camera (CCD72S, MTI-Dage, Michigan City, IN). The pixel size for all magnifications used was calibrated with a 100 lines/mm grating, which allowed for absolute distance measurements. The side length of the square image pixels was 118 ± 2 nm for the 40$\times$ objective with additional 2.5$\times$ magnification lens, used for the cell-size measurements. To measure larger distances, such as the distance between the fiber tip and the trapped object, we used a 20$\times$ objective, which resulted in an image pixel size of 611 ± 5 nm/pixel. All stretching experiments were done at room temperature.

Image analysis

After completing the experiments, image data were analyzed on a Macintosh computer to quantify the deformation of a cell in the optical stretcher. The algorithm was developed in the scientific programming environment MATLAB (MathWorks, Inc., Natick, MA), which treats bitmap images as matrices. Figure 5 *A* shows a typical phase contrast image of an RBC stretched at moderate light powers ($P \approx 100$ mW). The boundary of the cell in the image is the border between the dark cell and the bright halo. The goal was to extract the shape of the cell from this image to use the quantitative information for further evaluation.
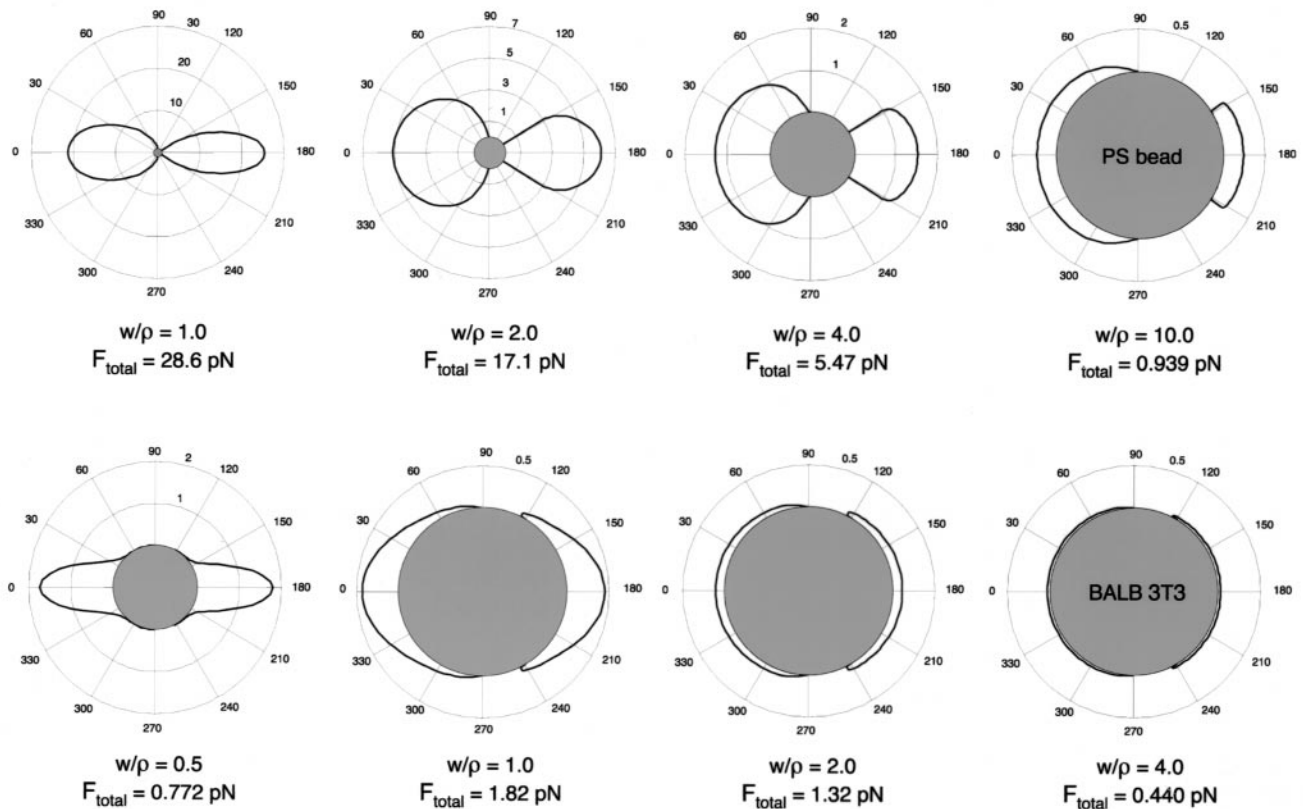
FIGURE 6   Surface stress profiles for one laser beam incident from the left on a polystyrene bead (*top row*) and a BALB 3T3 fibroblast (*bottom row*) for different ratios between the beam radius w and the object's radius ρ. The radii of the polystyrene bead and the fibroblast used for this calculation were $\rho = 2.55~\mu$m and $\rho = 7.70~\mu$m and the refractive indices were $n_2 = 1.610$ and $n_2 = 1.370$, respectively. The total light power $P = 100$ mW for all profiles. The concentric rings indicate the stress in Nm^{-2} (note the different scales). The resulting total force after integration over the surface acting on the center of gravity of the object is noted in each case.

The algorithm consists of the following steps. First, the geometrical center of the cell is found and used as the origin of a polar coordinate system. The grayscale values along the radii outward from the center are reassigned to Cartesian coordinates (see Fig. 5 *B*). Essentially, the image is cut along one radius and mapped onto a rectangle. The bottom of Fig. 5 *B* is the interior of the cell and the top is the outside. The cell boundary is along the wavy line between the black and the white bands. Next, the image is squared to enhance the contrast between cell and background. The effect of this filter can be seen in Fig. 5 *C*, which shows a line scan across the cell boundary. If we assume that the boundary between inside and outside coincides with the first peak, when moving from the outside to the inside of the cell, where the slope of the line scan is zero, we can drastically enhance the signal-to-noise ratio by dividing the data by their first spatial derivative. Because this would also enhance peaks in the background noise, we first threshold the image at a low value to set the background to zero. The combined effect of this mathematical filter can be seen in Fig. 5 *D*. The first peak, taken as the cell boundary, is then easy to detect (zigzag line in Fig. 5 *E*). The resolution up to this point is identical to the pixel resolution of the microscope/CCD system, i.e., 118 ± 2 nm/pixel. To further improve this resolution, we use the physical constraint that the cell boundary has to be smooth on this length scale. This is implemented by Fourier-decomposing the boundary data and by filtering out the high spatial frequency noise, which increases the resolution to an estimated ± 50 nm. The smooth line in Fig. 5 *E* is the inverse Fourier transform of

the remaining frequencies. The information about the deformation of cells is then extracted from the resulting function. Figure 5 *F* shows the original cell with the boundary as detected with this algorithm.

In general, this sort of image analysis can yield resolutions down to ± 11 nm (see, for example, Käs et al., 1996), which is well below the optical resolution of the microscope and also below the pixel resolution. The reason, in short, is that we do not want to resolve two close-by objects, which is limited to a distance of about half the wavelength. Instead, the goal is to detect how much an edge, characterized by a large change in intensity, is moving.

The absolute size determination of an object using this algorithm depends somewhat on the exact definition of the boundary between object and surrounding medium in the phase-contrast image. Our choice, as described above, was driven by the investigation of images of silica beads with known size. The estimated resolution of ± 50 nm is in agreement with measurements of these beads, which have a radius of $\rho = 2.50 \pm 0.04~\mu$m (SD). This resolution is certainly sufficient to discriminate between stretched and unstretched cells as reported further below. The advantages of this algorithm are its speed, precision, and its ability to detect the shape of any cell.

While the radii of the cells were measured with the algorithm, the distances between the fiber tip and the cell, d, were measured in a simpler way by counting pixels in images. For the $20\times$ objective, this can be done with a pixel resolution of $\pm 0.6~\mu$m.

RESULTS AND DISCUSSION

Theory

Total force for one beam

The simplest way to describe the interaction of light with cells is by ray optics (RO). This approach is valid when the size of the object is much larger than the wavelength of the light. The diameter of cells, 2ρ, is on the order of tens of microns. Cell biological experiments, such as the optical stretching of cells, are performed in aqueous solution, and water is sufficiently transparent only for electromagnetic radiation in the near infrared (the laser used was operated at a wavelength of $\lambda = 785$ nm). Thus, the criterion for ray optics, $2\pi\rho/\lambda \approx 25$–$130 \gg 1$, is fulfilled (van de Hulst, 1957).

The idea is to decompose an incident laser beam into individual rays with appropriate intensity, momentum, and direction. These rays propagate in a straight line in uniform, nondispersive media and can be described by geometrical optics. Each ray carries a certain amount of momentum p proportional to its energy E and to the refractive index n of the medium it travels in, $p = nE/c$, where c is the speed of light in vacuum (Ashkin and Dziedzic, 1973; Brevik, 1979). When a ray hits the interface between two dielectric media with refractive indices n_1 and n_2, some of the ray's energy is reflected. Let us assume that $n_2 > n_1$ and $n_2/n_1 \approx 1$, which is the case for biological objects in aqueous media, and that the incidence is normal to the surface. The fraction of the energy reflected is given by the Fresnel formulas (Jackson, 1975), $R \approx 10^{-3}$. The momentum of the reflected ray, $p_r = n_1 RE/c$, and the momentum of the transmitted ray, $p_t = n_2(1 - R)E/c$ (Ashkin and Dziedzic, 1973; Brevik, 1979). The incident momentum, $p_i = n_1 E/c$, has to be conserved at the interface. The difference in momentum between the incident ray and the reflected and transmitted rays, $\Delta p = p_i + p_r - p_t$, is picked up by the surface, which experiences a force F according to Newton's second law,

$$F = \frac{\Delta p}{\Delta t} = \frac{n_1 \Delta E}{c \Delta t} = \frac{n_1 QP}{c}, \qquad (1)$$

where P is the incident light power and Q is a factor that describes the amount of momentum transferred ($Q = 2$ for reflection, $Q = 1$ for absorption). For partial transmission of one laser beam hitting a flat interface at normal incidence as described above, $Q_{front} = 1 + R - n(1 - R) = -0.086$ ($n_1 = 1.33$, $n_2 = 1.43$, $n = n_2/n_1$). This force acts in the backward direction, away from the denser medium (see also Fig. 2). The transmitted ray eventually hits the backside of the object and again exerts a force on the interface. Here, $Q_{back} = [n + Rn - (1 - R)](1 - R) = 0.094$, and the force acts in the forward direction, again away from the denser medium. For the total force acting on the object's center of gravity, $Q_{total} = Q_{front} + Q_{back} = 0.008$. The total force is

obviously an order of magnitude smaller than either one of the surface forces.

If the ray hits the interface under an angle $\alpha \neq 0$, it changes direction according to Snell's law, $n_1\sin \alpha = n_2\sin \beta$, where β is the angle of the transmitted ray. In this case, the vector nature of momentum has to be taken into account and R becomes a function of the incident angle α. R is taken to be the average of the coefficients for perpendicular and parallel polarization relative to the plane of incidence. This is a negligible deviation from the true situation (the error in the stress introduced by this simplification is smaller than 2% for $n_2 = 1.45$, and smaller than 0.5% for $n_2 = 1.38$), but it simplifies the calculation and preserves symmetry of the problem with respect to the laser axis. The components of the force in terms of Q on the front side, parallel and perpendicular to the beam axis, are

$$
\begin{aligned}
Q_{front}^{parallel}(\alpha) &= \cos(0) - R\cos(\pi - 2\alpha) \\
&\quad - n(1 - R)\cos(2\pi - \alpha + \beta) \\
&= 1 + R(\alpha)\cos(2\alpha) \qquad (2a) \\
&\quad - n(1 - R(\alpha))\cos(\alpha - \beta) \\
&= Q_{front}(\alpha)\cos \phi,
\end{aligned}
$$

and

$$
\begin{aligned}
Q_{front}^{perpendicular}(\alpha) &= \sin(0) - R\sin(\pi - 2\alpha) \\
&\quad - n(1 - R)\sin(2\pi - \alpha + \beta) \\
&= R(\alpha)\sin(2\alpha) \qquad (2b) \\
&\quad + n(1 - R(\alpha))\sin(\alpha - \beta) \\
&= Q_{front}(\alpha)\sin \phi,
\end{aligned}
$$

where ϕ is the angle between the beam axis and the direction of the momentum transferred. Similarly, on the back the components of the surface force are

$$
\begin{aligned}
Q_{back}^{parallel}(\alpha) &= (1 - R(\alpha))[n\cos(\alpha - \beta) \\
&\quad + nR(\beta)\cos(3\beta - \alpha) \\
&\quad - (1 - R(\beta))\cos(2\alpha - 2\beta)] \quad (3a) \\
&= Q_{back}(\alpha)\cos \phi,
\end{aligned}
$$

and

$$
\begin{aligned}
Q_{back}^{perpendicular}(\alpha) &= (1 - R(\alpha))[-n\sin(\alpha - \beta) \\
&\quad + nR(\beta)\sin(3\beta - \alpha) \\
&\quad - (1 - R(\beta))\sin(2\alpha - 2\beta)] \quad (3b) \\
&= Q_{back}(\alpha)\sin \phi.
\end{aligned}
$$

Subsequent reflected and refracted rays can be neglected because $R < 0.005$ for all incident angles. The magnitude of the force in terms of Q on either the front or the backside is given by

$$Q_{\text{front/back}}(\alpha) = \sqrt{(Q_{\text{front/back}}^{\text{parallel}}(\alpha))^2 + (Q_{\text{front/back}}^{\text{perpendicular}}(\alpha))^2}, \quad (4)$$

which is a function of the incident angle α, and the direction of the force is

$$\phi_{\text{front/back}}(\alpha) = \arctan\left(\frac{Q_{\text{front/back}}^{\text{perpendicular}}(\alpha)}{Q_{\text{front/back}}^{\text{parallel}}(\alpha)}\right). \quad (5)$$

The forces on front and back are always normal to the surface for all incident angles. Thus, the stress σ, i.e., the force per unit area, along the surface where the ray enters and leaves the cell is

$$\sigma_{\text{front/back}}(\alpha) = \frac{F}{\Delta A} = \frac{n_1 Q_{\text{front/back}}(\alpha) I(\alpha)}{c}, \quad (6)$$

where $I(\alpha)$ is the intensity of the light. Figure 6 shows stress profiles calculated for spherical objects with the refractive index of polystyrene beads, and with the average refractive index of RBCs hit by one laser beam with Gaussian intensity distribution. The profiles are rotationally symmetric with respect to the beam axis. The sphere acts as a lens and focuses the rays on the back toward the beam axis, which results in a narrower stress profile. Integrating this asymmetrical stress over the whole surface yields the total force on the object's center of mass, which pushes the object in the direction of the beam propagation. At the same time, the applied stress stretches the object in both directions along the beam axis. Due to the cylindrical symmetry, the total force has only a component in the direction of the light propagation, which is generally called scattering force. If the object is displaced from the beam axis, this symmetry is broken. It experiences a force, called gradient force, perpendicular to the axis, which pulls the object toward the highest laser intensity at the center of the beam if the refractive index of the object is greater than that of the surrounding medium. Because the gradient force is restoring, after the object reaches the axis, it will stay there as long as no other external forces are present and the gradient force is zero.

The stress profile and the total force depend on the ratio between beam radius w and sphere radius ρ, and on the relative index of refraction, $n = n_2/n_1$. If there is only one beam shining on the object, the total force will accelerate it. Because the beam is slightly divergent (the beam radius doubles from $w = 2.7$ μm at the fiber tip to $w = 5.4$ μm over a distance of 70 μm), the beam radius w, and therefore the stress profiles and the total force, are functions of the distance d from the fiber end (see Fig. 8). Smaller beam size with respect to the object results in higher light intensity and thus greater stress on the surface ($w/\rho \ll 1$). As the beam

radius w increases with increasing distance d and w/ρ approaches one, the light intensity and the magnitude of the surface stress decrease. However, the total force increases because the asymmetry between the front and back becomes more pronounced. As the beam size becomes much larger than the object ($w/\rho \gg 1$), the surface stresses and the total force vanish, because less light is actually hitting the object. The highest total forces ($w/\rho = 1$) calculated for polystyrene beads in water and RBCs in their final buffer for a light power of $P = 100$ mW are $F_{\text{total}} = 28.6 \pm 0.9$ pN and $F_{\text{total}} = 1.82 \pm 0.06$ pN, respectively. The relative error in the force calculations, due to uncertainties in the measurement of the relevant quantities (indices of refraction, light power, radius, distance between fiber and object) as given earlier, is 3.2%. In general, the magnitude of the surface stress and the total force increase with higher relative indices of refraction n.

The change in total force as the object is pushed away from the light source can be measured by setting the accelerating total force F_{total} equal to the Stokes drag force acting on the spherical object,

$$F_{\text{total}} = 6\pi\eta\rho v, \quad (7)$$

where η is the viscosity of the surrounding medium and v is the velocity of the object. The viscous drag on a spherical object can depend strongly on the proximity of boundaries. A correction factor a can be found in terms of the ratio between the radius of the sphere ρ and the distance to the closest boundary b (Svoboda and Block, 1994),

$$a = \frac{1}{1 - \frac{9}{16}\frac{\rho}{b} + \frac{1}{8}\left(\frac{\rho}{b}\right)^3 - \frac{45}{256}\left(\frac{\rho}{b}\right)^4 - \frac{1}{16}\left(\frac{\rho}{b}\right)^5 + \cdots}. \quad (8)$$

The Reynolds number is on the order of 10^{-4}, so inertia can be neglected. The measurement of the total force on different objects was used to investigate to what extent cells can be approximated as objects with a homogeneous index of refraction (see Shooting Experiments).

Stress profiles for two beams

A configuration with two opposing, identical laser beams functions as a stable optical trap where the dielectric object is held between the two beams. When the object is trapped, the surface stresses caused by the two incident beams are additive. Fig. 7 shows the resulting stress profiles for RBCs, which are rotationally symmetric with respect to the beam axis. If the object is centered, the surface stresses cancel upon integration, and the total force is zero. Otherwise, restoring gradient and scattering forces will pull the object back into the center of the trap. The trapping force is the minimal force required to pull the object completely out of
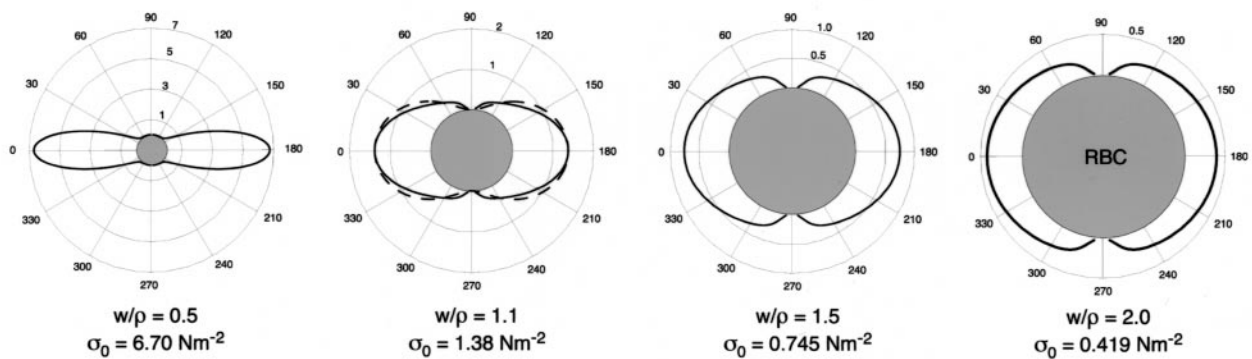
FIGURE 7 Surface stress profiles on an RBC trapped in the optical stretcher for different ratios between the beam radius w and the cell radius ρ. The total power in each beam was $P = 100$ mW for all profiles. The radius of the RBC used for this calculation was $\rho = 3.30$ μm, and the refractive index was $n_2 = 1.378$. The concentric rings indicate the stress in Nm^{-2}. The peak stresses σ_0 along the beam axis (0° and 180° direction) are given below each profile. The trapping of the cell for $w/\rho < 1$ is unstable (see text). The dashed line for $w/\rho = 1.1$ shows the $\sigma_r(\alpha) = \sigma_0\cos^2(\alpha)$ approximation of the true stress profile.

the trap, which is equal to the greatest gradient force encountered as the object is displaced.

Again, the shape of the profile changes depending on n and the ratio w/ρ. The smaller the beam size with respect to the object, the greater the stress in the vicinity of the axis. However, the trap is not stable if the beams are smaller than the object. This has been discussed and experimentally shown by Roosen (1977). For $w/\rho \gg 1$, the surface stresses become very small. The ideal trapping situation is when the beams are only slightly larger than the object ($w/\rho \geq 1$). For example, for $w/\rho = 1.1$, the peak stresses σ_0 along the beam axis for RBCs trapped with two 100-mW beams, $\sigma_0 = 1.38 \pm 0.05$ Nm^{-2}. The relative error in the stress calculations, due to uncertainties in the measurement of the relevant quantities as given earlier, is 3.0%. In this case, the stress profile can be well approximated by $\sigma_r(\alpha) = \sigma_0\cos^2(\alpha)$ (see Fig. 7 for $w/\rho = 1.1$). This functional form of the stress profile makes an analytical solution of the deformation of certain elastic objects tangible.

Deformation of thin shells

Erythrocytes were used initially because they are soft, easy to handle and to obtain, and their deformations are easily observed. They are also much more accessible to theoretical modeling than eukaryotic cells with their highly complex and dynamic internal structures. Thus, RBCs can be considered well-defined elastic objects that can be used to verify the calculated stress profiles. The only elastic component of RBCs is a thin composite shell made of the plasma membrane, the two-dimensional cytoskeleton, and the glycocalix. The ratio between shell radius ρ and shell thickness h, $\rho/h \approx 100$. In this case, membrane theory can

be used to describe deformations due to surface stresses (Mazurkiewicz and Nagorski, 1991; Ugural, 1999).

Membrane theory is the simplification of a more general theory of the deformation of spherical shells in which the bending energy U_b of the shell is neglected and only the membrane (or stretching) energy U_m is considered. It can be shown that the ratio of those two energies for the case of axisymmetric stress, as applied with the optical stretcher, is $U_b/U_m = 4h^2/3\rho^2 \approx 10^{-4}$ for RBCs. The stress σ_r applied to a spherical object in the optical stretcher has the form, $\sigma_r = \sigma_0\cos^2(\alpha)$, as shown above. Spherical coordinates are an obvious choice, where the radial direction is denoted by r, the polar angle by θ, and the azimuthal angle is ϕ. The coordinate system is oriented such that the incident angle of the rays, α, in the previous section is identical to the polar angle θ (the laser beams are traveling along the z-axis). The total energy U of a thin shell consists of the membrane energy and the work done by the stress applied and is given by,

$$U = 2\pi\rho^2 \int \left(\frac{Eh}{2(1 - \nu^2)} \left[\varepsilon_\theta^2 + \varepsilon_\phi^2 + 2\nu\varepsilon_\theta\varepsilon_\phi \right] \right. \tag{9}$$

$$\left. - \sigma_r u_r \times \sin(\theta) \right) d\theta,$$

where ϵ_θ and ϵ_ϕ are the strains in the polar and meridional direction, respectively, u_r is the radial deformation of the membrane, E is the Young's modulus, and ν is the Poisson ratio. The connections between the strains and the deformations are

$$\varepsilon_\theta = \frac{1}{\rho} \left(\frac{du_\theta}{d\theta} - u_r \right) \tag{10a}$$

and

$$\varepsilon_\phi = \frac{1}{\rho}(u_\theta \cot(\theta) - u_r), \tag{10b}$$

where u_θ is the deformation in meridional direction. The radial and meridional displacements, which describe the experimentally observed deformation of the dielectric object in the optical stretcher, can be found by using Euler's equations,

$$\frac{1}{\rho}\frac{d}{d\theta}\frac{dF}{du_\theta'} - \frac{dF}{du_\theta} = 0 \tag{11a}$$

and

$$\frac{1}{\rho}\frac{d}{d\theta}\frac{dF}{du_r'} - \frac{dF}{du_r} = 0, \tag{11b}$$

where F is the integrand of the energy functional,

$$u_\theta' = \frac{1}{\rho}\frac{du_\theta}{d\theta} \tag{12a}$$

and

$$u_r' = \frac{1}{\rho}\frac{du_r}{d\theta}. \tag{12b}$$

Using Eqs. 10, 11, and 12 and the explicit form of $\sigma_r(\theta)$, we find the following expressions for the radial and the meridional deformations of the membrane,

$$u_r(\theta) = \frac{\rho^2\sigma_0}{4Eh}[(5+v)\cos^2(\theta) - 1 - v] \tag{13a}$$

and

$$u_\theta(\theta) = \frac{\rho^2\sigma_0(1+v)}{2Eh}\cos(\theta)\sin(\theta). \tag{13b}$$

As expected from the symmetry of the problem, the deformations u_r and u_θ are independent of the azimuthal angle ϕ, and there is also no displacement u_ϕ in this direction. Figure 11 shows the shapes of thin shells calculated with Eq. 13a for $v = 0.5$, which is normal for biological membranes, and $Eh = (3.9 \pm 1.4) \times 10^{-5}$ Nm^{-1}, which was found to be the average for RBCs from the experiments (see below) for increasing stresses σ_0. Because these equations are linear, they only hold for small strains (<10%). In the microscope images, which are cross-sections of the objects because the focal depth of the objective is much smaller than the diameter of the RBCs, only the radial deformations can be observed. The direct comparison between the theoretically expected deformations $u_r(\theta)$ and the experimentally observed radial deformations help to establish the RO model as valid explanation for the optical stretching of soft dielectric objects.

Experiments

Shooting experiments

To test the assumptions underlying the RO calculations as described above, we measured the total force acting on different objects. It was not clear if it was permissible to model living cells with their organelles and other small-scale structures as homogeneous spheres with an isotropic index of refraction. Although this assumption is obvious for RBCs homogeneously filled with hemoglobin, it might be questionable in the case of eukaryotic cells containing organelles and other internal structures (see Fig. 3). In this series of experiments, individual silica beads, polystyrene beads, or fibroblasts were trapped in the optical stretcher. The setup was identical to the one used for the trapping and stretching of RBCs (see Experimental Setup and Fig. 4). After stably trapping the objects, we blocked one of the laser beams. The total force from the other beam accelerated the object away from the light source.

The total force was determined using Eqs. 7 and 8 and the velocities, radii, and distances measured during the experiment. In our setup, the distance b between the moving objects and the coverslip as closest boundary was $b = 62.5 \pm 2.5 \mu$m (half the diameter of the optical fiber). In the case of the silica and polystyrene beads, this distance is about 25 times the radius of the beads and the correction factor $a = 1.023$. For the cells, the distance is ~7–9 times the radius and $a = 1.072$–1.090. The viscosity η used in the calculation was that for water at 25°C, $\eta = 0.001$ Pa s. Figure 8 shows the total force measured as a function of the distance d between the fiber tip and the object, as well as the total force as expected from our RO calculations. The error bars shown are statistical errors in the experimental data. The relative errors introduced by the uncertainties in the measurements of radii, velocities, and distances are negligibly small (1.1–3.1%). It is not surprising that the experimental data points for silica beads and polystyrene beads match the theory because these are truly spherical and have an isotropic index of refraction. The fact that, also, the experimental results for the cells matched the theory was proof that even eukaryotic cells can be treated using this simple RO model. The magnitude and the dependence of the total force on the distance d are in good agreement with the results by (Roosen, 1977).

Stretching of erythrocytes

Single, osmotically swollen RBCs were trapped in the optical stretcher at low light powers ($P \approx 5$–10 mW). The light power was then increased to a higher value between $P = 10$ and $P = 800$ mW for approximately 5 s, an image of the stretched cell was recorded, and the light power was decreased again to the original value. During the short time intervals when stress was applied, we did not observe any creep, i.e., any increase in deformation during the duration
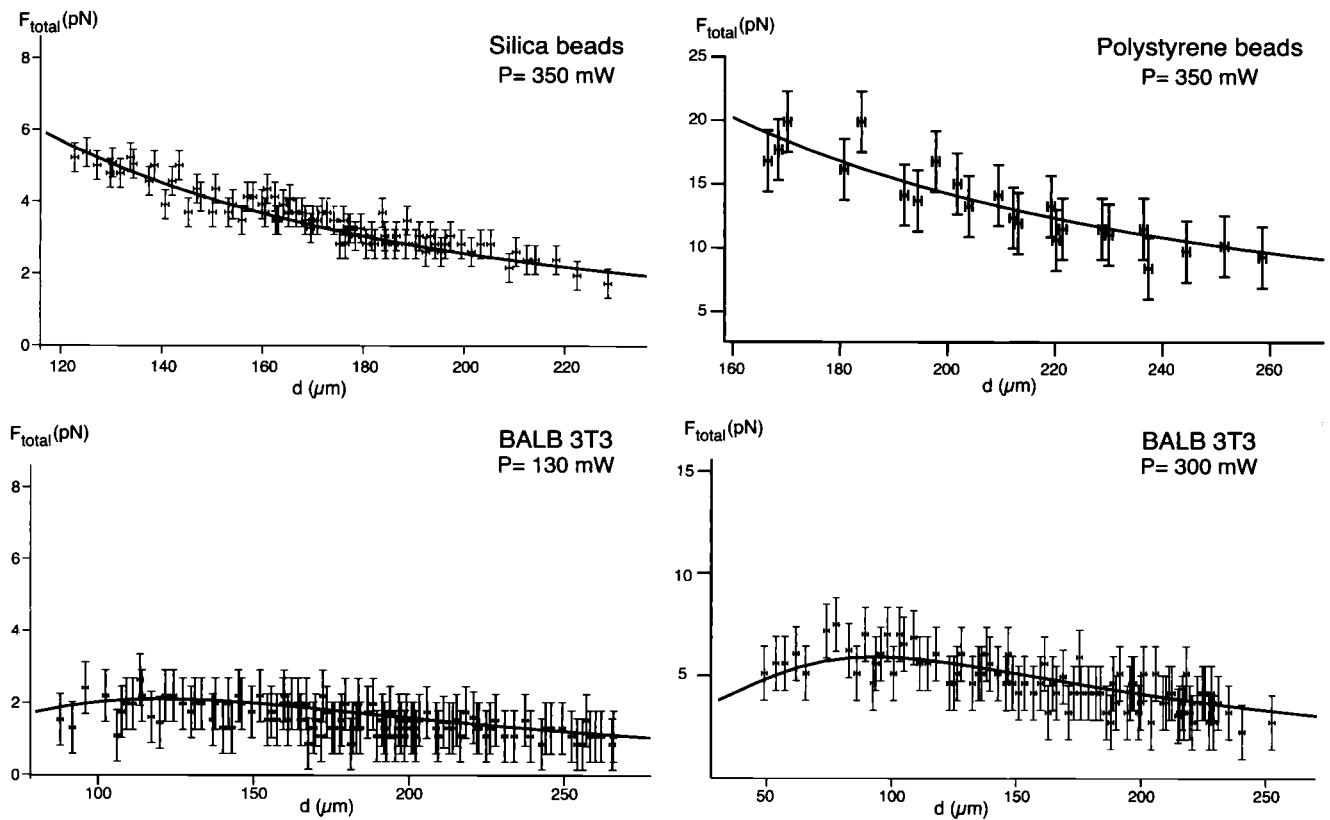
FIGURE 8 The total forces from one laser beam on silica beads, polystyrene beads, and BALB 3T3 fibroblasts as functions of the distance d between the fiber tip and the object. The data points are from measuring the total force on the objects in the optical stretcher after obstructing one of the laser beams. The solid lines represent the total forces calculated using ray optics. The radii of the silica beads, the polystyrene beads, and the fibroblasts were $\rho = 2.50 \pm 0.04$ μm, $\rho = 2.55 \pm 0.04$ μm, and $\rho = 7.70 \pm 0.05$ μm, and the refractive indices were $n_2 = 1.430 \pm 0.003$, $n_2 = 1.610 \pm 0.005$, and $n_2 = 1.370 \pm 0.005$, respectively. The total light power P is indicated in each case. The error bars represent standard deviations; the error in the distance measurement was ± 0.6 μm.

of the stretching. Also, the cells did not show any hysteresis or any kind of plastic deformation up to $P \approx 500$ mW. Figure 9 shows a sequence of RBC images recorded at increasing light powers. It is obvious that the deformation increased with the light power used. The radius along the beam axis increased from 3.13 ± 0.05 μm in the first image to 3.57 ± 0.05 μm in the last image, a relative increase of $14.1 \pm 0.3\%$, whereas the radius in the perpendicular direction decreased from 3.13 ± 0.05 μm to 2.77 ± 0.05 μm (relative change $-11.5 \pm 0.2\%$).

From the radius of the cell, the distance between cell and fiber tips, the refractive indices of cell and medium, and the power measured, we calculated the stress profiles for each cell using the RO model. As mentioned earlier, the relative error in the stress calculation is 3.0%. The peak stress in the last image of Fig. 9 was calculated as $\sigma_0 = 1.47 \pm 0.03$ Nm^{-2}. Figure 10 shows the relative increase in radius along the beam axis ($\theta = 0$) and the relative decrease perpendicular ($\theta = \pi/2$) versus the peak stress σ_0 for 55 RBCs. The error bars shown are statistical errors. The relative errors in the calculation of the relative changes and the peak stresses due to uncertainties in the relevant quantities measured are

comparatively small. The solid line in Fig. 10 shows a fit of $u_r(0)/\rho$ (see Eq. 13a) to the experimental data. For the fit, the errors in the peak stresses were neglected and a singular value decomposition algorithm was used. The data points were weighed with the inverse of the standard deviations. The resulting slope was 0.080 ± 0.011 m^{2}N^{-1}, which yielded $Eh = (3.9 \pm 1.4) \times 10^{-5}$ Nm^{-1}. The intercept was zero. The correlation coefficient for the fit was, $r = 0.92$, excluding the last data point. This shows that up to $\sigma_0 \approx 2$ Nm^{-2} ($P \approx 350$ mW) and relative deformations of about 10%, the response of the RBCs was linear. In this regime, linear membrane theory can be used to describe the deformation of RBCs.

In the literature, usually the cortical shear modulus Gh is given, rather than the Young's modulus Eh. The quantities are related by $Gh = Eh/2(1 + \nu) = Eh/3$. In our case, the shear modulus, $Gh = (1.3 \pm 0.5) \times 10^{-5}$ Nm^{-1}. This value is in good agreement with values reported previously from micropipette aspiration measurements, which yielded shear moduli in the range 6–9×10^{-6} Nm^{-1} (Hochmuth, 1993). Micropipette aspiration is the most established technique for measuring cellular elasticities, and the value for the shear
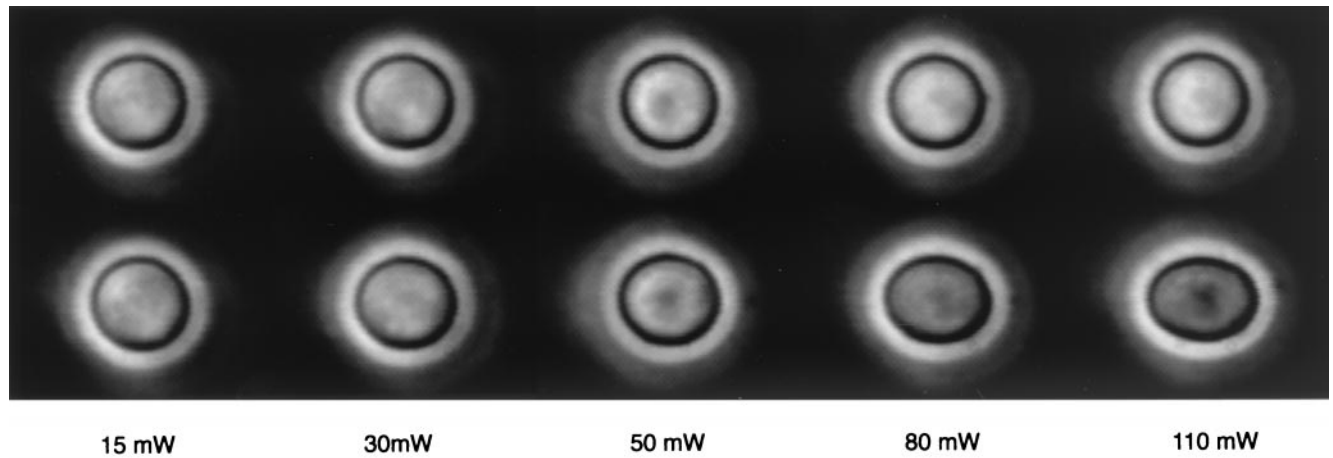
FIGURE 9 Typical sequence of the stretching of one osmotically swollen RBC for increasing light powers. The top row shows the RBC trapped at 5 mW in each beam. The power was then increased to the higher power given below, which lead to the stretching shown underneath, and then reduced again to 5 mW. The stretching clearly increases with increasing light power. The radius of the unstretched cell was $\rho = 3.13 \pm 0.05$ μm, and the distance between the cell and either fiber tip was $d \approx 60$ μm. The images were obtained with phase contrast microscopy. Any laser light was blocked by an appropriate filter.

modulus of the RBC membrane has been confirmed many times and is well accepted.

More recently, optical tweezers were used to measure the shear modulus with very differing results. In these experi-ments, beads were attached to the membrane on opposite sides of the RBC, trapped with optical tweezers, and then displaced. The values found ranged from $(2.5 \pm 0.4) \times 10^{-6}$ Nm^{-1} (Hénon et al., 1999) to 2×10^{-4} Nm^{-1} (Sleep et al.,
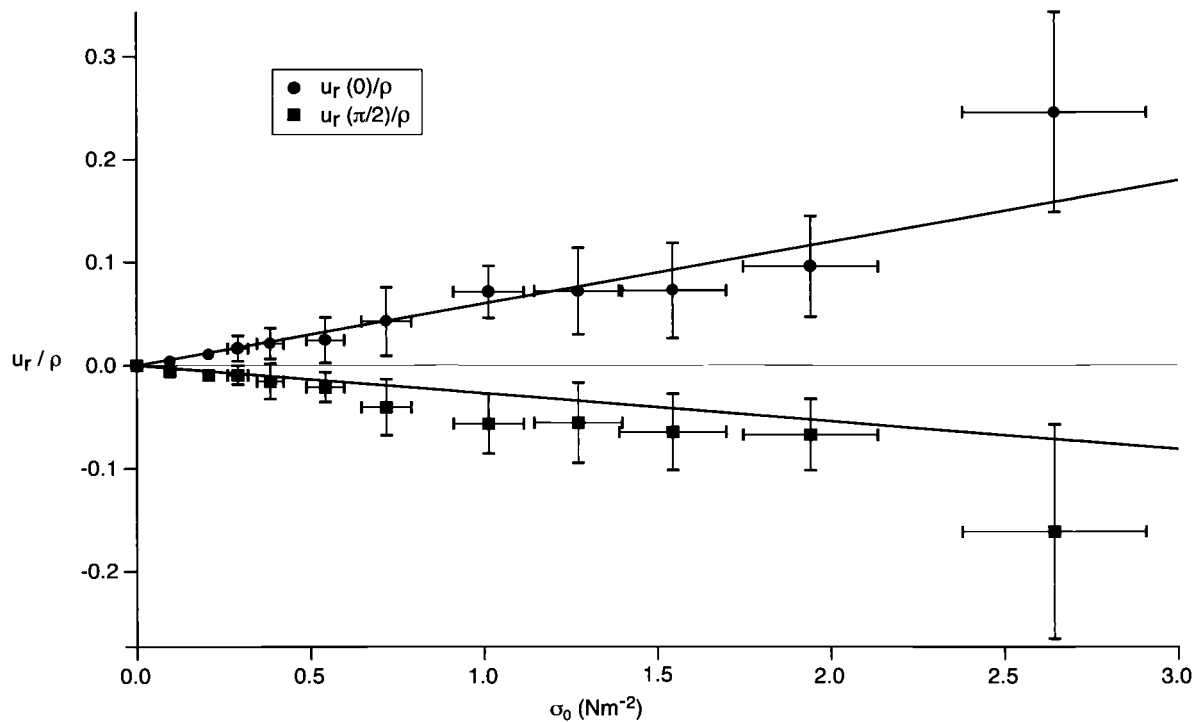

FIGURE 10 Relative deformation u_r/ρ of RBCs along (*positive values*) and perpendicular (*negative values*) to the laser axis in the optical stretcher as a function of the peak stress σ_0. The error bars for the relative deformations and the peak stresses are standard deviations. The solid line shows a fit of Eq. 13a as derived from membrane theory to the data points using a singular value decomposition algorithm. The linear correlation coefficient for this fit, $r = 0.92$, (excluding the last data point) indicates a linear response of the RBCs to the applied stress. Beyond a peak stress $\sigma_0 \approx 2$ Nm^{-2} the deformation starts deviating from linear behavior.

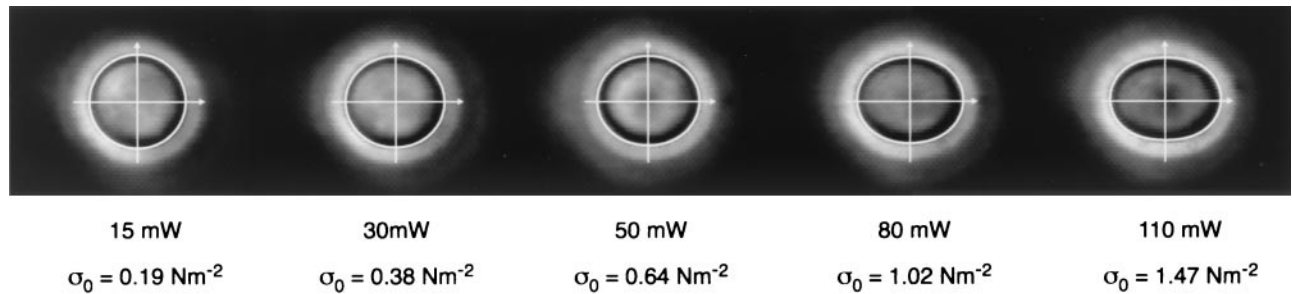| 15 mW	30mW	50 mW	80 mW	110 mW
$\sigma_0 = 0.19$ Nm^{-2}	$\sigma_0 = 0.38$ Nm^{-2}	$\sigma_0 = 0.64$ Nm^{-2}	$\sigma_0 = 1.02$ Nm^{-2}	$\sigma_0 = 1.47$ Nm^{-2}

FIGURE 11 Comparison between the deformations of RBCs observed in the optical stretcher and the deformations expected from membrane theory (*white lines*). The peak stresses σ_0 calculated using ray optics, which are shown with each image, were used for the membrane theory calculations. The resulting theoretical shapes, calculated with Eq. 13a, were overlaid on the original images from Fig. 9 to show the excellent agreement between the two for all peak stresses.

1999). Because this technique applies point forces to the membrane, the stress is highly localized and leads to non-linear deformations. The discrepancy between these values and the established values for the shear modulus can probably be attributed to this different load condition.

Furthermore, the theoretically expected and the observed shapes of RBCs in the optical stretcher coincide well (see Fig. 11). The white lines are the shapes of thin shells with RBC material properties as predicted by linear membrane theory subjected to the surface profile calculated by the RO model. These lines were overlaid on the images of the stretched RBCs in Fig. 9. The excellent agreement between the predicted and the observed shaped shows that using RO theory is sufficient to calculate the surface stress on cells in the optical stretcher. An ab inito treatment of the interaction of a spherical dielectric object in an inhomogeneous electromagnetic wave using Maxwell's equations and surface stress tensor would be much more difficult and is also not necessary in this case. The RO model is powerful enough to accurately predict the qualitative and the quantitative aspect of the stretching. Ray optics has the additional benefit of being much more accessible.

Beyond $\sigma_0 \approx 2$ Nm^{-2}, the response of the RBCs became nonlinear and the shapes observed began to diverge from the ones expected from the linear membrane theory. Figure 12 shows the response of such a cell. At a peak stress of $\sigma_0 = 2.55 \pm 0.10$ Nm^{-2}, the cell was stretched from a radius along the beam axis of 3.36 ± 0.05 μm to 6.13 ± 0.05 μm (relative change $82 \pm 3\%$), whereas the perpendicular radius decreased from 3.38 ± 0.05 μm to 2.23 ± 0.05 μm (relative change $-34 \pm 2\%$). For the same cell, this transition from linear to nonlinear response was repeatable several times. Due to the variance in age, size, and elasticity between individual cells, the point of transition differed between different cells. If stretched even further (beyond $\sigma_0 \approx 3$ Nm^{-2}), the cells would rupture, as proven by the visually detectable release of hemoglobin from the cells.

Stretching of eukaryotic cells

Similar to most eukaryotic cells, BALB 3T3 fibroblasts are heavily invested by an extensive 3D cytoskeletal network of polymeric filaments, mainly actin filaments, which is largely preserved even in the suspended state (see below). Because these cells resemble solid spheres made of a non-

FIGURE 12 An example of an RBC stretched beyond the linear regime. The top part shows the undeformed cell trapped at 5 mW with a radius $\rho = 3.36 \pm 0.05$ μm. In the lower part, the cell is stretched with a peak stress $\sigma_0 \approx 2.55 \pm 0.10$ Nm^{-2} to $\rho = 6.13 \pm 0.05$ μm along the beam axis, an increase of $82 \pm 3\%$. After reducing the power, the cell returned to its original shape.
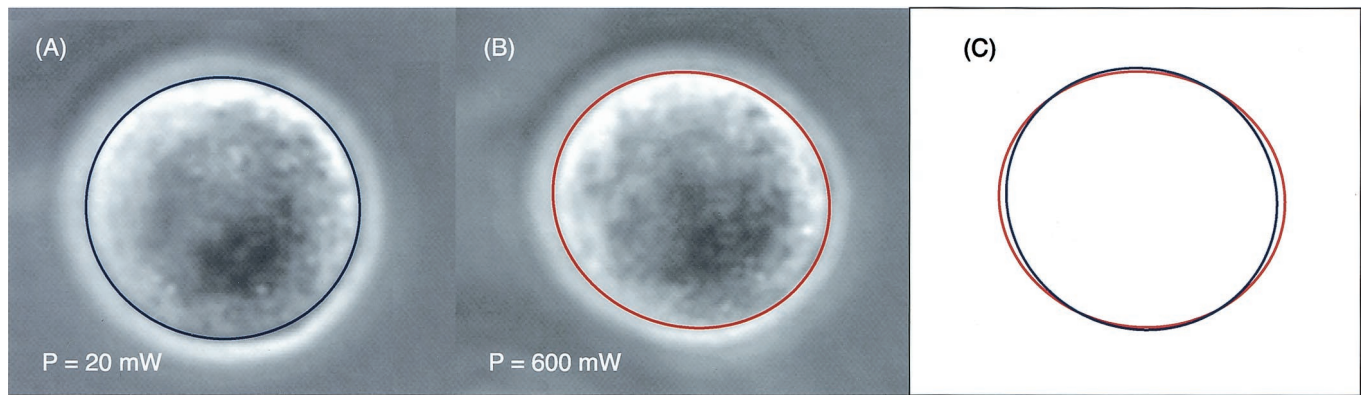
FIGURE 13 The stretching of a BALB 3T3 fibroblast in the optical stretcher. Due to the more extensive cytoskeleton of eukaryotic cells, the deformation is less obvious than for the RBCs. Still, the radius increased from (*A*) $\rho = 11.23 \pm 0.05$ μm for the cell trapped at 20 mW to (*B*) $\rho = 11.84 \pm 0.05$ μm along the beam axis at 600 mW, and decreased from 11.53 ± 0.05 μm to 11.27 ± 0.05 μm in the perpendicular direction. This is a relative deformation of $5.43 \pm 0.04\%$ and $-2.25 \pm 0.01\%$, respectively, for a peak stress $\sigma_0 = 5.3 \pm 0.2$ Nm^{-2}. The deformation can be seen much easier in (*C*) where the outlines of the stretched and unstretched cell, found with the image analysis algorithm, are overlaid.

uniform, complex compound material, we expected that they would not be stretched as significantly as RBCs, which are essentially thin shells. Figure 13 shows a fibroblast (*A*) trapped at $P = 20$ mW light power and (*B*) stretched with $P = 600$ mW. The peak stress in this case was, $\sigma_0 = 5.3 \pm 0.2$ Nm^{-2}, and the relative deformation along the beam axis was $5.43 \pm 0.04\%$, and $-2.25 \pm 0.01\%$ in the perpendicular direction. The small degree of deformation of this fibroblast is only possible to detect by using the algorithm for the extraction of the cell boundary (*C*). Any eukaryotic cell can be stretched this way. Although the applied stress can be calculated and the resulting deformation of cells can be measured, it would be incorrect to calculate a Young's modulus assuming a homogeneous elastic sphere. It would require complex modeling and probably time dependent measurements to extract elastic properties of the different cytoskeletal components.

Viability of stretched cells

The viability of the cells under investigation was an important issue because dead cells do not maintain a representative cytoskeleton. Even though care had been taken to avoid radiation damage to cells in the optical stretcher by selecting a wavelength (785 nm) with low absorption, their viability was checked on a case-by-case basis. Our approach to this was twofold. The appearance of BALB 3T3 cells is significantly different when they are not alive. Living cells in phase contrast microscopy show a characteristic bright rim around their edge. Dead cells usually have no sharp contour and appear diffuse. After a cell had been trapped and stretched for several minutes, it was compared with other cells that had not been irradiated. In all cases, the cells looked alike and normal. A second, more careful approach was the use of the vital stain Trypan Blue. As long as a cell is alive, it is able to prevent the dye from entering the

cytoplasm. When the cell is dead or does not maintain its normal function, the dye will penetrate the cell membrane and the whole cell appears blue. After adding 5% (volume) Trypan Blue to the cell suspension, no staining was observed. These tests show that the cells survived the conditions in an optical stretcher without any detectable damage.

It is not obvious that it is possible to use two 800-mW laser beams for the deformation of such delicate objects as cells without causing radiation damage. An important consideration is the careful choice of the least damaging wavelength. For the trapping of inanimate matter, such as glass or silica beads, the choice of wavelength is not critical. Using a short wavelength might be desirable for optical tweezers because it results in higher gradients and better trapping efficiencies because the spot size of a focused beam is about half the wavelength of the light used. However, short wavelengths are not appropriate to preserve biological objects such as cells because the absorption by chromophores in cells is low in the infrared and increases with decreasing wavelength (Svoboda and Block, 1994). The absorption peaks of proteins, for example, are found in the ultraviolet region of the electromagnetic spectrum. Therefore, researchers resorted to the 1064 nm of an Nd-YAG laser and achieved better results (Ashkin et al., 1987). At first sight, this choice seems also less than optimal because 70% of a cell's weight is water (Alberts et al., 1994), which absorbs more strongly with increasing wavelength. Most cells trapped with optical tweezers do not survive light powers greater than 20–250 mW, depending on the specific cell type and the wavelength used (Ashkin et al., 1987; Ashkin and Dziedzic, 1987; Kuo and Sheetz, 1992). However, recent work on optical tweezers shows that local heating of water can be ruled out as limiting factor in optical trapping experiments in the near infrared region. Theoretical calculations predict a temperature increase of less than 3 K/100 mW in the wavelength range 650-1050 nm for durations of

up to 10 s (Schönle and Hell, 1998). This is in agreement with earlier experimental work, where an average temperature increase of $<1.00 \pm 0.30°C/100$ mW at powers up to 400 mW was observed in Chinese hamster ovary cells (CHO cells) trapped in optical tweezers at a wavelength of 1064 nm (Liu et al., 1996).

Even though heating due to water absorption seems to be unimportant in trapping experiments, the cells could still be damaged by radiation in other ways. Studies directly monitoring metabolic change and cellular viability of biological samples trapped in optical tweezers addressed this concern. Microfluorometric measurements on CHO cells (Liu et al., 1996) show that up to 400 mW of 1064-nm cw laser light does not change the DNA structure or cellular pH. Still, the right choice of wavelength is important, because rotating *E. coli* assays reveal that there is photodamage with maxima at 870 and 930 nm and minima at 830 and 970 nm (Neuman et al., 1999). There seems to be evidence that the presence of oxygen is involved in the damage pathway but the direct origin of the damage remains unclear. According to this study, damage at 785 nm, the wavelength we used, is at least as small as at 1064 nm, the most commonly used wavelength for biological trapping experiments. Also, the sensitivity to light was found to be linearly related to the intensity, which rules out multi-photon processes.

In the light of these findings, it is not surprising that we did not observe any damage to the cells trapped and stretched in the optical stretcher. This becomes even more plausible if one considers that the beams are not focused and the power densities are lower than in optical tweezers by about two orders of magnitude for the same light power ($\sim 10^5$ rather than 10^7 W/cm^2). Thus, much higher light powers, i.e., higher forces, can obviously be used without the danger of "optiction".

Cytoskeleton of cells in suspension

Finally, because there was some concern that eukaryotic cells, apart from leukocytes, might dissolve their actin cytoskeleton when they are in suspension, we examined the actin cytoskeleton of BALB 3T3 fibroblasts in suspension using TRITC-phalloidin labeling and fluorescence microscopy. Figure 14 clearly shows that suspended cells do have an extensive actin network throughout the whole cell. In particular, the peripheral actin cortex can be seen at the plasma membrane. The only features of the cytoskeleton not present in suspension are stress fibers, which is consistent with the absence of focal adhesion plaques in suspended cells. Even without stress fibers, the BALB 3T3 displayed a large resistance to deformation in the optical stretcher. Stress fibers are predominantly seen in cells adhered to a substrate and are less pronounced in cells embedded in a tissue matrix. Thus, the situation with many stress fibers is probably as unphysiologic as the lack thereof in suspended cells.
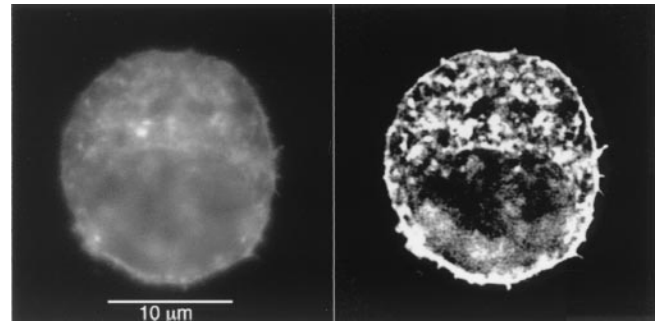

FIGURE 14   Fluorescence image of a BALB 3T3 fibroblast in suspension. The cell had been fixed and the actin cytoskeleton labeled with TRITC-phalloidin. The left panel shows the original image and the right panel shows the same cross-section through the cell after deconvolution. Clearly, the cell maintains a filamentous actin cytoskeleton even in suspension.

Our finding is in agreement with other studies that report the disappearance of stress fibers and a redistribution of actin. Furthermore, these studies show that the influence of the cytoskeleton on the deformability of normally adherent cells such as bovine aortic endothelial cells (Sato et al., 1987), chick embryo fibroblasts (Thoumine and Ott, 1997), and rat embryo fibroblasts (Heidemann et al., 1999) can be investigated when the cells are in suspension.

This view is supported by recent frequency-dependent AFM microrheology experiments, comparing in vitro actin gels and NIH3T3 fibroblasts (Mahaffy et al., 2000). These experiments showed that the viscoelastic signature of the cells resembled that of homogeneous actin gels, so that the elastic strength of cells can be almost entirely attributed to the actin cortex, which is still present in suspended cells. There is actually an advantage to investigating cells in suspension, because most polymer theories are for in vitro, isotropic actin networks. It might be especially interesting to be able to compare these theories with data from living cells in which only the actin cortex is present and anisotropic structures such as stress fibers are absent.

CONCLUSION AND OUTLOOK

Although the possibility of optically trapping biological matter with lasers is well known and commonly used, the optical deformability of dielectric matter had been ignored. The optical stretcher proves to be a nondestructive optical tool for the quantitative deformation of cells. The forces exerted by light due to the momentum transferred are sufficient not only to hold and move objects, but also to directly deform them. The important point is that the momentum is predominantly transferred to the surface of the object. The total force, i.e., gradient and scattering force, which traps the object, arises from the asymmetry of the resulting surface stresses when the object is displaced from its equilibrium position and acts on the center of gravity of

the object. These trapping forces are significantly smaller than the forces on the surface because the surface forces almost completely cancel upon integration. This is most obvious in a two-beam trap as used for the optical stretcher. When the dielectric object is in the center of the optical trap, the total force is zero, whereas the forces on the surface can be as high as several hundred pico-Newton. In synopsis, the forces applicable for cell elasticity measurements with the optical stretcher range from those possible with conventional optical tweezers to those achieved with atomic force microscopes.

Somewhat surprising was the finding that the surface forces pull on the surface rather than compressing it. The RO approach readily explains this behavior by the increase of the light's momentum as it enters the denser medium and the resulting stresses on the surface. An equivalent approach would be to think in terms of minimization of energy. It is energetically favorable for a dielectric object to have as much of its volume located in the area with the highest intensity along the laser beam axis. The result is that the cell is pulled toward the axis. Even though this is conceptionally correct, it would be much harder to calculate.

The optical deformability of cells can be used to distinguish between different cells by detecting phenomenological differences in their elastic response as demonstrated for RBCs and BALB 3T3 fibroblasts. At the same time, trapped cells did not show any sign of radiation damage, even when stretched with up to 800 mW of light in each beam, and maintained a representative cytoskeleton in suspension. In the same way, the optical stretcher can be used for quantitative research on the cytoskeleton. For example, it is commonly believed that the actin part of the cytoskeleton, and especially the actin cortex, is most important for the elasticity of the cell. This hypothesis can be easily tested using the optical stretcher to measure the elasticity after genetically altering the relative amount of the three different main cytoskeletal components and their accessory proteins.

There might also be a biomedical application of the optical stretcher. Due to its simple setup and the incorporation of an automated flow chamber, the optical stretcher has the potential to measure the elasticity of large numbers of cells in a short amount of time. We expect to be able to measure one cell per second, which is a large number of cells compared to existing methods for measuring cell elasticity. Given the limited lifespan of a living cell sample in vitro, the measurement frequency is crucial to ensure good statistics. This naturally suggests the optical stretcher for applications in the research and diagnosis of diseases that result in abnormalities of the cytoskeleton. Better knowledge of the basic cell biology of the cytoskeleton contributes to the understanding of these disorders and can affect diagnosis and therapy of these diseases. Cytoskeletal changes are significant in, and are even used to diagnose, certain diseases such as cancer. Existing methods of cancer detection rely on markers and optical inspection (Sidransky,

1996). Using measurements of cytoskeletal elasticity as an indicator for malignancy could be a novel approach in oncology. For example, effects of malignancy on the cytoskeleton that have been reported include increasing disorder of the actin cytoskeleton (Koffer et al., 1985; Takahashi et al., 1986), changes in the absolute amount of total actin and the relative ratio of the various actin isoforms (Wang and Goldberg, 1976; Goldstein et al., 1985; Leavitt et al., 1986; Takahashi et al., 1986; Taniguchi et al., 1986), an overexpression of gelsolin in breast cancer cells (Chaponnier and Gabbiani, 1989), and the lack of filamin in human malignant melanoma cells (Cunningham et al., 1992). All of these changes will likely result in an altered viscoelastic response of these cells that can be detected with the optical stretcher. In fact, models of actin networks (MacKintosh et al., 1995) show that the shear modulus scales with actin concentration raised to 2.2. Even a slight decrease in actin concentration should result in a detectable decrease of the cell's elasticity. In this way, the optical stretcher could advance to a diagnostic tool in clinical laboratories. This novel technique would require minimal tissue samples, which could be obtained using cytobrushes on the surfaces of the lung, esophagus, stomach, or cervix, or by fine-needle aspiration using stereotactic, ultrasonographic, or MRI guidance (Dunphy and Ramos, 1997; Fajardo and DeAngelis, 1997).

REFERENCES

Adelman, M. R., G. G. Borisy, M. L. Shelanski, R. C. Weisenberg, and E. W. Taylor. 1968. Cytoplasmic filaments and tubules. *Fed. Proc.* 27:1186–1193.

Aebi, U., J. Cohn, L. Buhle, and L. Gerace. 1986. The nuclear lamina is a meshwork of intermediate-type filaments. *Nature.* 323:560–564.

Alberts, B., D. Bray, J. Lewis, M. Raff, K. Roberts, and J. D. Watson. 1994. Molecular Biology of the Cell. Garland Publishing, New York. 786–861.

Allen, P. G., and P. A. Janmey. 1994. Gelsolin displaces phalloidin from actin filaments. A new fluorescence method shows that both Ca^{2+} and Mg^{2+} affect the rate at which gelsolin severs F-actin. *J. Biol. Chem.* 269:32916–32923.

Ashkin, A. 1970. Acceleration and trapping of particles by radiation pressure. *Phys. Rev. Lett.* 24:156–159.

Ashkin, A., and J. M. Dziedzic. 1973. Radiation pressure on a free liquid surface. *Phys. Rev. Lett.* 30:139–142.

Ashkin, A., and J. M. Dziedzic. 1987. Optical trapping and manipulation of viruses and bacteria. *Science.* 235:1517–1520.

Ashkin, A., J. M. Dziedzic, J. E. Bjorkholm, and S. Chu. 1986. Observation of a single-beam gradient force optical trap for dielectric particles. *Opt. Lett.* 11:288–290.

Ashkin, A., J. M. Dziedzic, and T. Yamane. 1987. Optical trapping and manipulation of single cells using infrared laser beams. *Nature.* 330:769–771.

Barer, R., and S. Joseph. 1954. Refractometry of living cells, part I. Basic principles. *Q. J. Microsc. Sci.* 95:399–423.

Barer, R., and S. Joseph. 1955a. Refractometry of living cells, part II. The immersion medium. *Q. J. Microsc. Sci.* 96:1–26.

Barer, R., and S. Joseph. 1955b. Refractometry of living cells, part III. Technical and optical methods. *Q. J. Microsc. Sci.* 96:423–447.

Bennett, V. 1985. The membrane skeleton of human erythrocytes and its implication for more complex cells. *Annu. Rev. Biochem.* 54:273–304.

Bennett, V. 1990. Spectrin-based membrane skeleton—a multipotential adapter between plasma membrane and cytoplasm. *Physiol. Rev.* 70:1029–1060.

Block, S. M., L. S. B. Goldstein, and B. J. Schnapp. 1990. Bead movement by single kinesin molecules studied with optical tweezers. *Nature.* 348:348–352.

Brevik, I. 1979. Experiments in phenomenological electrodynamics and the electromagnetic energy-momentum tensor. *Phys. Rep.* 52:133–201.

Carlier, M. F. 1998. Control of actin dynamics. *Curr. Opin. Cell Biol.* 10:45–51.

Carlson, R. H., C. V. Gabel, S. S. Chan, R. H. Austin, J. P. Brody, and J. W. Winkelman. 1997. Self-sorting of white blood cells in a lattice. *Phys. Rev. Lett.* 79:2149–2152.

Chaponnier, C., and G. Gabbiani. 1989. Gelsolin modulation in epithelial and stromal cells of mammary carcinoma. *Am. J. Pathol.* 134:597–603.

Chu, S. 1991. Laser manipulation of atoms and particles. *Science.* 253:861–866.

Colon, J. M., P. G. Sarosi, P. G. McGovern, A. Ashkin, and J. M. Dziedzic. 1992. Controlled micromanipulation of human sperm in three dimensions with an infrared laser optical trap: effect on sperm velocity. *Fertil. Steril.* 57:695–698.

Constable, A., J. Kim, J. Mervis, F. Zarinetchi, and M. Prentiss. 1993. Demonstration of a fiber-optical light-force trap. *Opt. Lett.* 18:1867–1869.

Cooper, J. A., J. Bryan, B. Schwab, III, C. Frieden, D. J. Loftus, and E. L. Elson. 1987. Microinjection of gelsolin into living cells. *J. Cell Biol.* 104:491–501.

Cunningham, C. C., J. B. Gorlin, D. J. Kwiatkowski, J. H. Hartwig, P. A. Janmey, H. R. Byers, and T. P. Stossel. 1992. Actin-binding protein requirement for cortical stability and efficient locomotion. *Science.* 255:325–327.

Dailey, B., E. L. Elson, and G. I. Zahalak. 1984. Cell poking. Determination of the elastic area compressibility modulus of the erythrocyte membrane. *Biophys. J.* 45:661–682.

Discher, D. E., N. Mohandas, and E. A. Evans. 1994. Molecular maps of red cell deformation: hidden elasticity and in situ connectivity. *Science.* 266:1032–1035.

Dunphy, C., and R. Ramos. 1997. Combining fine-needle aspiration and flow cytometric immunophenotyping in evaluation of nodal and extranodal sites for possible lymphoma: a retrospective review. *Diagn. Cytopathol.* 16:200–206.

Eichinger, L., B. Köppel, A. A. Noegel, M. Schleicher, M. Schliwa, K. Weijer, W. Wittke, and P. A. Janmey. 1996. Mechanical perturbation elicits a phenotypic difference between dictyostelium wild-type cells and cytoskeletal mutants. *Biophys. J.* 70:1054–1060.

Elson, E. L. 1988. Cellular mechanics as an indicator of cytoskeletal structure and function. *Annu. Rev. Biophys. Biophys. Chem.* 17:397–430.

Evans, E., and Y. C. Fung. 1972. Improved measurements of the erythrocyte geometry. *Microvasc. Res.* 4:335–347.

Fajardo, L. L., and G. A. DeAngelis. 1997. The role of stereotactic biopsy in abnormal mammograms. *Surg. Oncol. Clin. North Am.* 6:285–299.

Felder, S., and E. L. Elson. 1990. Mechanics of fibroblast locomotion: quantitative analysis of forces and motions at the leading lamellas of fibroblasts. *J. Cell Biol.* 111:2513–2526.

Guck, J., R. Ananthakrishnan, T. J. Moon, C. C. Cunningham, and J. Käs. 2000. Optical deformability of soft biological dielectrics. *Phys. Rev. Lett.* 84:5451–5454.

Goldstein, D., J. Djeu, G. Latter, S. Burbeck, and J. Leavitt. 1985. Abundant synthesis of the transformation-induced protein of neoplastic human fibroblasts, plastin, in normal lymphocytes. *Cancer Res.* 45:5643–5647.

Heidemann, S. R., S. Kaech, R. E. Buxbaum, and A. Matus. 1999. Direct observations of the mechanical behaviors of the cytoskeleton in living fibroblasts. *J. Cell Biol.* 145:109–122.

Hénon, S., G. Lenormand, A. Richert, and F. Gallet. 1999. A new determination of the shear modulus of the human erythrocyte membrane using optical tweezers. *Biophys. J.* 76:1145–1151.

Herrmann, H., and U. Aebi. 1998. Structure, assembly, and dynamics of intermediate filaments. *Subcell. Biochem.* 31:319–362.

Hochmuth, R. M. 1993. Measuring the mechanical properties of individual human blood cells. *J. Biomech. Eng.* 115:515–519.

Jackson, J. D. 1975. Classical Electrodynamics. John Wiley and Sons, New York. 281–282.

Janmey, P. A. 1991. Mechanical properties of cytoskeletal polymers. *Curr. Opin. Cell Biol.* 3:4–11.

Janmey, P. A., V. Euteneuer, P. Traub, and M. Schliwa. 1991. Viscoelastic properties of vimentin compared with other filamentous biopolymer networks. *J. Cell Biol.* 113:155–160.

Janmey, P. A., J. Peetermans, K. S. Zaner, T. P. Stossel, and T. Tanaka. 1986. Structure and mobility of actin filaments as measured by quasielastic light scattering, viscometry, and electron microscopy. *J. Biol. Chem.* 261:8357–8362.

Janmey, P. A., J. V. Shah, K. P. Janssen, and M. Schliwa. 1998. Viscoelasticity of intermediate filament networks. *Subcell. Biochem.* 31:381–397.

Käs, J., H. Strey, J. X. Tang, D. Finger, R. Ezzell, E. Sackmann, and P. A. Janmey. 1996. F-actin, a model polymer for semiflexible chains in dilute, semidilute, and liquid crystalline solutions. *Biophys. J.* 70:609–625.

Koffer, A., M. Daridan, and G. Clarke. 1985. Regulation of the microfilament system in normal and polyoma virus transformed cultured (BHK) cells. *Tissue Cell.* 17:147–159.

Kuo, S. C., and M. P. Sheetz. 1992. Optical tweezers in cell biology. *Trends Cell Biol.* 2:116–118.

Kuo, S. C., and M. P. Sheetz. 1993. Force of single kinesin molecules measured with optical tweezers. *Science.* 260:232–234.

Leavitt, J., G. Latter, L. Lutomski, D. Goldstein, and S. Burbeck. 1986. Tropomyosin isoform switching in tumorigenic human fibroblasts. *Mol. Cell. Biol.* 6:2721–2726.

Liu, Y., G. J. Sonek, M. W. Berns, and B. J. Tromberg. 1996. Physiological monitoring of optically trapped cells: assessing the effects of confinement by 1064-nm laser tweezers using microfluorometry. *Biophys. J.* 71:2158–2167.

Lodish, H., D. Baltimore, A. Berk, S. L. Zipurski, P. Matsudaira, and J. Darnell. 1995. Molecular Cell Biology. Scientific American Books, New York. 1051–1059.

MacKintosh, F. C., J. Käs, and P. A. Janmey. 1995. Elasticity of semiflexible biopolymer networks. *Phys. Rev. Lett.* 75:4425–4428.

Mahaffy, R. E., C. K. Shih, F. C. MacKintosh, and J. Käs. 2000. Scanning probe-based frequency-dependent microrheology of polymer gels and biological cells. *Phys. Rev. Lett.* 85:880–883.

Mazurkiewicz, Z. E., and R. T. Nagorski. 1991. Shells of Revolution. Elsevier Publishing, New York. 360–369.

Mitchison, T., L. Evans, E. Schulze, and M. Kirschner. 1986. Sites of microtubule assembly and disassembly in the mitotic spindle. *Cell.* 45:515–527.

Mitchison, T. J. 1992. Compare and contrast actin filaments and microtubules. *Mol. Biol. Cell.* 3:1309–1315.

Mohandas, N., and E. Evans. 1994. Mechanical properties of the red cell membrane in relation to molecular structure and genetic defects. *Annu. Rev. Biophys. Biomol. Struct.* 23:787–818.

Neuman, K. C., E. H. Chadd, G. F. Liou, K. Bergman, and S. M. Block. 1999. Characterization of photodamage to *Escherichia coli* in optical traps. *Biophys. J.* 77:2856–2863.

Pasternak, C., and E. L. Elson. 1985. Lymphocyte mechanical response triggered by cross-linking surface receptors. *J. Cell Biol.* 100:860–872.

Petersen, N. O., W. B. McConnaughey, and E. L. Elson. 1982. Dependence of locally measured cellular deformability on position on the cell, temperature, and cytochalasin B. *Proc. Natl. Acad. Sci. U.S.A.* 79:5327–5331.

Pollard, T. D. 1984. Molecular architecture of the cytoplasmic matrix. *Kroc Found. Ser.* 16:75–86.

Pollard, T. D. 1986. Assembly and dynamics of the actin filament system in nonmuscle cells. *J. Cell. Biochem.* 31:87–95.

Radmacher, M., M. Fritz, C. M. Kacher, J. P. Cleveland, and P. K. Hansma. 1996. Measuring the viscoelastic properties of human platelets with the atomic force microscope. *Biophys. J.* 70:556–567.

Roosen, G. 1977. A theoretical and experimental study of the stable equilibrium positions of spheres levitated by two horizontal laser beams. *Opt. Commun.* 21:189–195.

Rotsch, C., and M. Radmacher. 2000. Drug-induced changes of cytoskeletal structure and mechanics in fibroblasts: an atomic force microscopy study. *Biophys. J.* 78:520–535.

Sato, M., M. J. Levesque, and R. M. Nerem. 1987. An application of the micropipette technique to the measurement of the mechanical properties of cultured bovine aortic endothelial cells. *J. Biomech. Eng.* 109:27–34.

Schönle, A., and S. W. Hell. 1998. Heating by absorption in the focus of an objective lens. *Opt. Lett.* 23:325–327.

Shepherd, G. M., D. P. Corey, and S. M. Block. 1990. Actin cores of hair-cell stereocilia support myosin motility. *Proc. Natl. Acad. Sci. U.S.A.* 87:8627–8631.

Sidransky, D. 1996. Advances in cancer detection. *Sci. Am.* 275:104–109.

Simmons, R. M., J. T. Finer, H. M. Warrick, B. Kralik, S. Chu, and J. A. Spudich. 1993. Force on single actin filaments in a motility assay measured with an optical trap. *In* The Mechanism of Myofilament Sliding in Muscle Contraction. H. Sugi and G. H. Pollack, editors. Plenum, New York. 331–336.

Sleep, J., D. Wilson, R. Simmons, and W. Gratzer. 1999. Elasticity of the red cell membrane and its relation to hemolytic disorders: an optical tweezers study. *Biophys. J.* 77:3085–3095.

Stossel, T. P. 1984. Contribution of actin to the structure of the cytoplasmic matrix. *J. Cell Biol.* 99:15s–21s.

Stossel, T. P., J. H. Hartwig, P. A. Janmey, and D. J. Kwiatkowski. 1999. Cell crawling two decades after Abercrombie. *Biochem. Soc. Symp.* 65:267–280.

Strey, H., M. Peterson, and E. Sackmann. 1995. Measurements of erythrocyte membrane elasticity by flicker eigenmode decomposition. *Biophys. J.* 69:478–488.

Svoboda, K., and S. M. Block. 1994. Biological applications of optical forces. *Annu. Rev. Biophys. Biomol. Struct.* 23:147–285.

Svoboda, K., C. F. Schmidt, B. J. Schnapp, and S. M. Block. 1993. Direct observation of kinesin stepping by optical trapping interferometry. *Nature.* 365:721–727.

Tadir, Y., W. H. Wright, O. Vafa, T. Ord, R. H. Asch, and W. M. Berns. 1990. Force generated by human sperm correlated to velocity and determined using a laser generated optical trap. *Fertil. Steril.* 53:944–947.

Takahashi, K., V. I. Heine, J. L. Junker, N. H. Colburn, and J. M. Rice. 1986. Role of cytoskeleton changes and expression of the H-ras oncogene during promotion of neoplastic transformation in mouse epidermal JB6 cells. *Cancer Res.* 46:5923–5932.

Taniguchi, S., T. Kawano, T. Kakunaga, and T. Baba. 1986. Differences in expression of a variant actin between low and high metastatic B16 melanoma. *J. Biol. Chem.* 261:6100–6106.

Thoumine, O., and A. Ott. 1997. Time scale dependent viscoelastic and contractile regimes in fibroblasts probed by microplate manipulation. *J. Cell Sci.* 110:2109–2116.

Ugural, A. C. 1999. Stresses in Plates and Shells. McGraw-Hill, New York. 339–409.

van de Hulst, H. C. 1957. Light Scattering by Small Particles. John Wiley and Sons, New York. 172–176.

Wang, E., and A. R. Goldberg. 1976. Changes in microfilament organization and surface topography upon transformation of chick embryo fibroblasts with Rous sarcoma virus. *Proc. Natl. Acad. Sci. U.S.A.* 73:4065–4069.

Wang, N., J. P. Butler, and D. E. Ingberg. 1993. Mechanotransduction across the cell surface and through the cytoskeleton. *Science.* 260:1124–1127.

Wang, N., and D. Stamenovic. 2000. Contribution of intermediate filaments to cell stiffness, stiffening, and growth. *Am. J. Physiol. Cell Physiol.* 279:C188–C194.

Zeman, K. 1989. Untersuchung physikalisch und biochemisch induzierter Änderungen der Krümmungselastizität der Erythrozytenmembran mittels Fourierspektroskopie der thermisch angeregten Oberflächenwellen (Flickern). Doktorarbeit. Physikalische Fakultät, Technische Universität München, Germany.